FULL PAPER

Open Access

Paleomagnetic study of basaltic rocks from Baengnyeong Island, Korea: efficiency of the Tsunakawa–Shaw paleointensity determination on non-SD-bearing materials and implication for the early Pliocene geomagnetic field intensity

Hyeon-Seon Ahn[1*] and Yuhji Yamamoto[2]

Abstract

Finding the statistical intensity signatures of the Earth's magnetic field over geologic time has helped understanding of the evolution of the Earth's interior and its interactions with other integral parts of Earth systems. However, this has been often hampered by a paucity of absolute paleointensity (API) data, which are difficult to obtain primarily because of non-ideal magnetic behaviors of natural materials. Here, we present new API determination data with paleodirectional and rock magnetic analyses from basaltic rocks probably aged ~4–5 Ma in Baengnyeong Island, Korea. Paleodirectional analysis obtained an overall mean direction of $D = 347.3°$ and $I = 38.3°$ ($a_{95} = 4.9°$, $k = 113.4$) corresponding to a virtual geomagnetic pole at 342.1° E and 70.2° N. Comprehensive rock magnetic analyses identified Ti-poor titanomagnetite with, in part, multi-domain (MD) particles as a main carrier of remanent magnetization. The Tsunakawa–Shaw (TS) method yielded 12 qualified API estimates with a high success rate, efficiently removing possible MD influences, and resulted in a mean value of 13.1 μT with good precision (1.7 μT, standard deviation). The Thellier method of the IZZI protocol with pTRM checks, coupled with the use of a bootstrap approach instead of the "conventional best-fitting" in API determination, gave 6.6–19.7 μT as a 95% confidence interval of its mean API estimate, which supports the reliability of our TS-derived API mean estimate; but it is not considered in the final mean value because of the relatively large uncertainty. The virtual dipole moment corresponding to the TS-derived API mean, 2.9 ($\pm$0.4) $\times 10^{22}$ Am^2, is somewhat lower than the expectations of the past few Myr averages. Combined with a global API database, our new data implies a larger dispersion in the dipole moment during the early Pliocene than previously inferred. This also suggests that the issue of whether the early Pliocene average dipole strength was moderately high (>5 $\times 10^{22}$ Am^2) or consistent (4–5 $\times 10^{22}$ Am^2) should be discussed further.

Keywords: Baengnyeong island, Early pliocene, Paleomagnetism, Non-SD-bearing material, Tsunakawa–Shaw paleointensity, Thellier-type paleointensity

*Correspondence: mitsuki_ahs@hotmail.com; hs.ahn@kigam.re.kr
[1] Geological Research Center, Geology Division, Korea Institute of Geoscience and Mineral Resources (KIGAM), Daejeon 34132, Republic of Korea
Full list of author information is available at the end of the article

Introduction

The history of Earth can be investigated by seeking its magnetic field evolution, which is associated with the evolution of its deep interior (Gubbins and Richards 1986; Gubbins 1988; Glatzmaier et al. 1999; Roberts and Glatzmaier 2000; Costin and Buffett 2004; Biggin et al. 2015; Tarduno et al. 2015) but may also interact with other integral parts of the Earth system on variable geological time scales (Courtillot et al. 2007; Tarduno et al. 2007; Lee and Kodama 2009; Tarduno et al. 2010; Kitaba et al. 2012, 2017). For a complete picture of the geomagnetic field over time, it is clearly useful to acquire directions and intensities of the surface paleomagnetic field from geological materials (paleomagnetic full-vector data).

However, geological and experimental alterations of materials often create non-ideal magnetic properties as less suitable magnetic recorders, which often prohibits estimation of such paleofield directions and intensities. This has led, to date, to a sparsity (in terms of geological time and space) of reliable paleomagnetic data, of highly variable quantity and quality, over. In particular, such a limitation is more conspicuous in absolute paleointensity (API) data, which often leads to inconsistent views about the time-averaged statistical signature of the geomagnetic field on million year (Myr) timescales and its temporal evolution (e.g. McFadden and McElhinny 1982; Goguitchaichvili et al. 1999 versus Juarez and Tauxe 2000; Cromwell et al. 2015 for the past few Myr). Despite the significant effort by many paleomagnetists over the world, the temporal coverage of API data is concentrated into the past few Myr, dropping sharply at ~4 million years ago (Ma) and for older periods. In East Asia, particularly, the paucity of data becomes evident for time periods older than ~1 Ma. In the case of PINT (version 2015.05; http://earth.liv.ac.uk/pint/, accessed July, 2018; see Biggin and Paterson (2014)), a global API database, the number of API data (N_{API}) for the past 4 Myr is 1730 (40%) out of 4293 with data populations of 144–1059 per 1 Myr (/Myr), which is much higher compared than the < 100/Myr in the other older periods, and in East Asia (100–150° E; N_{API} = 387, 9% of the total) the data populations for the past 1 Myr and the other order periods are 138/Myr and < 55/Myr, respectively.

Recently, a number of API studies (Yamamoto and Tsunakawa 2005; Ziegler et al. 2011; Cromwell et al. 2015; Wang et al. 2015) have found that the axial dipole moments of the geomagnetic field during periods of the Plio–Pleistocene, on average, were approximately 4–5×10^{22} Am^2. Furthermore, integrating results from some previous studies (Goguitchaichvili et al. 2003; Pan et al. 2005; Lhuillier et al. 2019) could suggest that a moderately high state of the dipole strength, at least as high as

$\sim 6 \times 10^{22}$ Am^2, lasted for an approximately long geologic period from the Middle–Late Miocene (~10 Myr length). However, due to the paucity of qualified API data, how long-term field structures change between the Late Miocene and the Pliocene remains unclear.

In fact, the determination of API is much more difficult and time-consuming than determining field direction. Researchers have developed a variety of methods for API determination with different theoretical/experimental protocols and conditions, and material types and sizes. These are mostly targeting API determinations in blocking temperature (T_b) space. For bulk rock samples, the Thellier-type methods have been classically the most frequently utilized with various experimental conditions and protocols (Thellier and Thellier 1959; Coe 1967; Aitken et al. 1988; Riisager and Riisager 2001; Tauxe and Staudigel 2004; Wang and Kent 2013); however, they are prone to high failure rates for API determination due to non-ideal behaviors in the experiments, such as sagged (or curved or concave-up), kinked, zigzagged, and S-shaped patterns in the Arai diagram (Nagata et al. 1963; the plot of natural remanent magnetization (NRM) remaining versus laboratory-induced thermoremanent magnetization (TRM) gained).

Generally, ideal materials for API determination are rare in nature. Thus, a number of additional experimental protocols have been suggested: the "pTRM check" (where pTRM denotes partial TRM; Prévot et al. 1985), the "pTRM-tail check" (Riisager and Riisager 2001), the "IZZI protocol" (Tauxe and Staudigel 2004; Yu et al. 2004) for detecting and rejecting non-ideal results, and the second API experiment that uses a lab simulated NRM proposed by Wang and Kent (2013) for correcting non-ideal results arising from multi-domain (MD) magnetic particles. The additional protocols have enhanced the number of reliable API data, but there is still a limitation; whichever of the above protocols are used, it is still time-consuming and subject to moderate rates of acquisition of reliable API determinations. As a different approach, Bowles et al. (2005) and Shaar et al. (2011) utilized a new bootstrap procedure instead of the conventional best-fitting line procedure for determining an API estimate in MD-like curved Arai plots; it is based on the observation that two "end-case" slopes in the curved Arai diagram can provide adequate constraints for the true API value. It has the potential to enhance the acquisition rate of meaningful API values with Thellier-based methods, although interpretation should be careful.

An alternative promising technique is to obtain API data in coercivity (H_c) space: one of such techniques with a high success rate even from non-ideal materials is the Tsunakawa–Shaw method (Tsunakawa and Shaw 1994; Yamamoto et al. 2003; Mochizuki et al. 2004; Oishi et al.

2005; also called "LTD-DHT Shaw method"). This technique is the most advanced variant of the Shaw method (Shaw 1974) coupled with ARM correction, low-temperature demagnetization (LTD) treatment, and a double heating test (DHT). It can detect and even correct for non-ideal behaviors in the associated results and generate a qualified API estimate by the following procedure: selective demagnetization of MD-like remanence by the LTD treatment (Yamamoto et al. 2003), correction for laboratory thermal alteration by anhysteretic remanent magnetization (ARM) (Rolph and Shaw 1985), and checking the validity of the ARM correction by DHT (Tsunakawa and Shaw 1994). Successful applications of the method have been validated in historical lava flows in Japan and Hawaii (Yamamoto et al. 2003; Mochizuki et al. 2004; Oishi et al. 2005; Yamamoto and Hoshi 2008). Furthermore, for old volcanic rocks and burnt archeological materials, the method has yielded indistinguishable API estimates from those obtained by the Thellier-type methods (Yamamoto et al. 2010; Ahn et al. 2016; Kitahara et al. 2018; Yamamoto and Yamaoka 2018).

In this study, we report new API data from early Pliocene volcanic units ("Jinchon Basalt", ~4–5 Ma) in Baengnyeong Island, Korea, to fill the gap in the current global API database. Analyzed samples, containing MD magnetic minerals, are taken from two units of the same age (statistically indistinguishable from each other). We apply not only the Tsunakawa–Shaw method (hereafter referred to as the 'TS method') but also the Thellier method of the IZZI protocol (hereafter referred to as the 'IZZI-T' method) with pTRM checks. An additional use of a bootstrap approach in API determination is adapted to a result obtained by the IZZI-T method to compare with and examine the TS determination. Combining the API results by the TS method and the IZZI—T method, we can have a robust API estimate in the early Pliocene.

Brief geological background and samples

Late Cenozoic alkali magmatism in East Asia is known to originate in the shallow asthenosphere, largely in response to dramatic changes in stress regimes, which resulted from the interplay between the India-Eurasia collision and subduction of the Pacific Plate beneath the eastern margin of Eurasia (Choi et al. 2006). The associated basaltic rocks, with estimated ages in the Mio-Pliocene, are sparsely distributed in South Korea (Fig. 1a) and include Baengnyeong Island (~4–7 Ma; Kim et al. 2005; Choi et al. 2006), the Goseong area (~6–7 Ma; Choi et al. 2006), Pyeongtaek-Asan area (~14–19 Ma; Shin et al. 2006), Boun area (~11 Ma; Arai et al. 2001), and Ulsan-Gyeongju area (~16–22 Ma; Jin et al. 1988). Many outcrops of these Mio-Pliocene basaltic rocks still need more accurate and precise geochronological constraints.

Baengnyeong Island (37° 55′ N, 124° 40′ E) is 45 km^2 in area and is situated off the furthest northwest point of South Korea (Fig. 1a). Part of the tectonic regime of the Korean Peninsula, the island lies within the Phanerozoic Imjingang Belt, which is in contact with the Precambrian Gyeonggi Massif (or Gyeonggi Block) to the south and the Precambrian Nangrim Massif (or Nangrim Block) to the north and has been considered the eastern extension of the collision zone between the North China Block and the South China Block (or between the North Sino-Korea Block and the South Sino-Korea Block) (Chough et al. 2000). Figure 1b shows a simplified geological map of Baengnyeong Island (modified from Park and Park 1996; Lim et al. 1999). The oldest strata of the island, which are the majority, are composed of Proterozoic metasedimentary rocks (slate, phyllite, and quartzite). The Proterozoic strata are intruded by dioritic dikes of unknown age (presumably Late Cretaceous to Paleogene). The middle part of the island is covered by Quaternary alluvium and beach sand layers. In the northeastern part of the island, Neogene intrusive and extrusive volcanic rocks are exposed covering ~4 km^2, called Jinchon Basalt, which have been previously reported to have a variety of compositions, including alkali basalt, trachybasalt, basanite, and phonotephrite in Park and Park (1996) and Choi et al. (2006), and even basaltic andesite and basaltic trachyandesite in Kim et al. (2002). The Jinchon Basalt rocks contain mantle-derived spinel peridotite xenoliths (Park and Park 1996; Choi and Kwon 2005; Choi et al. 2005). For the host rocks there are documentations of whole-rock K–Ar ages: 4.2 ± 0.1 (1σ) Ma for basanite (Choi et al. 2006), 6.4 ± 0.2 (1σ) Ma for phonotephrite, and 7.1 ± 0.3 (1σ) Ma for basaltic andesite (Kim et al. 2005).

For two Jinchon Basalt rock sites named B1 and B2 along the coast of the exposures, 7 oriented block samples each were collected in 2007 (collectively 14 block samples). The distance between these two sites is ~0.3 km. Relationship between the two exposures (e.g. the same versus different cooling units?) remained uncertain in the field observation due to the discontinuity spacing of the exposures. The sampled sites were regarded as the same place, or very close, to where the K–Ar age of ~4.2 Ma was assigned by Choi et al. (2006). It is also said to be ~5 Ma or so for the age of the exposures by unpublished radiometric age data (personal communication with Dr. Youn Soo Lee of Pohang University of Science and Technology). Considering the uncertainty of age determination for now, we thus assign ~4–5 Ma as a tentative age of our sampled rocks. The orientation was made using a magnetic compass equipped with a tripod. A lack of bias to the needle of the magnetic compass influenced by the basalt outcrops was confirmed by monitoring the declination changes of the compass needle while moving in
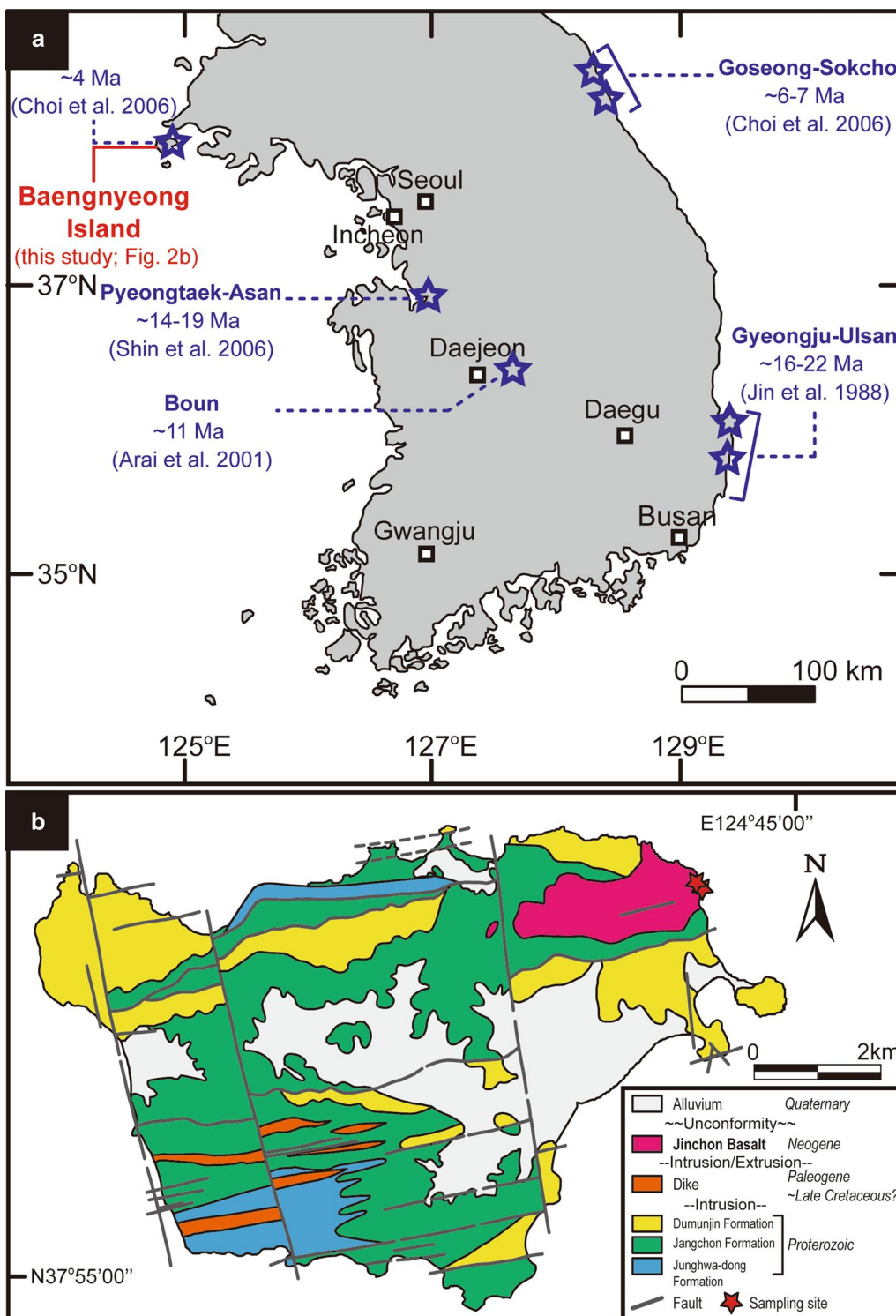
Fig. 1 Location and simplified geologic map of the studied area. **a** Distribution of locations of volcanic rocks with Miocene to Early Pliocene ages in South Korea, with available radiometric age estimates and their reference literatures and location of this study area (Baengnyeong Island). **b** Geologic map of Baengnyeong Island (after Park and Park 1996; Lim et al. 1999), with locations of our sampling sites, which belong to the Jinchon Basalt

lines perpendicular to the outcrop planes. At the laboratory of the Center for Advanced Marine Core Research (CMCR), Kochi University, Japan, multiple cylindrical specimens 25 mm in diameter and ~ 12–22 mm in height were prepared from each of the collected samples. For these specimens, name of a specimen consists of site name, block sample code, and core and specimen (subcore) numbers (for example, specimen B1A-1-1 means that he site name is B1, the block sample code is A, and the following 1-1 is core and specimen numbers). In addition, multiple small fragments (tiny subsamples), a few tens of mg in weight, were selectively prepared from each of the drilled long cylindrical subsamples. Naming of these fragment specimens are similar as the above case for the cylindrical specimens (but, sometime, the specimen number was used to be omitted in the specimen name; see Fig. 2a–c).

Methods

Rock magnetic and paleomagnetic experiments conducted in this study were conducted at the CMCR laboratory of Kochi University.

Measurements of rock magnetic properties

Using a MPMS-XL5 magnetic property measurement system (Quantum Design), remanence measurements at low temperatures were performed on powdered subsamples prepared from the small fragments with two different experimental sequences: (1) thermal demagnetization during zero-field warming (ZFW) of an isothermal remanence (IRM) imparted with a 2.5 T field at 10 K after zero-field cooling (ZFC) from 300 K (ZFC remanence) and (2) thermal demagnetization during ZFW of a remanence taken during cooling from 300 to 10 K with a field of 2.5 T (FC remanence). Additionally, the temperature dependence of low-field magnetic susceptibility was measured at 1, 10, 100, and 1000 Hz.

Using an NMB-89 magnetic balance (Natsuhara Giken), a small fragment of each sample was subjected to high-temperature thermomagnetic analyses, where it was heated from the room temperature (~ 20 °C) to 700 °C and then cooled to 50 °C, in a constant applied field of 0.5 T and an average heat rate of ~ 10 °C/min, under the ambient air environment.

Using a MicroMag 3900 vibrating sample magnetometer (VSM; Princeton Measurements Corporation), a magnetic hysteresis loop and determinations of hysteresis parameters (saturation magnetization, Ms; saturation remanent magnetization, Mrs; coercive force, Bc; and coercivity of remanence, Bcr) were each made on a chip subsample, with a maximum applied field of 0.5 T. Then, with the VSM, 263 first-order reversal curves (FORCs) were also measured at an averaging time of 100 ms applying a maximum applied field of 1 T. The FORCs were analyzed with the FORCinel software (Harrison and Feinberg 2008) and the results displayed on a FORC diagram.

Paleomagnetic direction analyses

A suite of NRM measurements and alternating field (AF) demagnetizations were performed on prepared cylindrical specimens using a DSPIN automated spinner magnetometer equipped with an AF demagnetizer (Natsuhara Giken). Prior to the AF procedure, each specimen was subjected to LTD treatment, in which the specimen was placed in a dewar bottle filled with liquid nitrogen and the assemblage kept in a Mu-metal shield space (near-zero-field) for 10 min and then left at the room temperature for approximately 30 min in the zero field. The AF demagnetizations (AFDs) were set to 34 steps in peak fields from 2 to 140 mT. These 11 LTD-AFD-treated specimens were afterwards used in the Tsunakawa–Shaw PI experiments. For directional analyses, compass readings of the sample orientation were corrected for the site declination of the present-day Earth's magnetic field of − 8°. The progressive demagnetization data for each specimen were identified with the orthogonal vector diagram of Zijderveld (1967) and equal-area projection. To determine particular directions of remanent magnetizations for each specimen-level demagnetization data, principal component analysis (PCA) was performed applying the Kirschvink method (1980). If necessary, the great-circle-fit technique (Kirschvink 1980) was also used for direction determination. Mean directions for the determined remanence components were calculated using Fisherian statistics (Fisher 1953).

API determination

Tsunakawa–Shaw (TS) method

For 21 prepared cylindrical specimens from the two sites, the TS API experiments were conducted following a procedure similar to the one described in Yamamoto and Tsunakawa (2005). Remanence measurements, AFD treatments, and acquisitions of anhysteretic remanent magnetization (ARM) were made using the DSPIN automated system. AFD treatments all were performed with 34 (or 38) steps in the peak AFs from 2 to 140 (or 180) mT. All ARMs were imparted by a direct current (DC) bias field of 50 mT with the peak AFs of 180 mT, in which the bias field directions were (sub-)parallel to the characteristic directions of NRM or laboratory-induced TRM directions. In acquiring the laboratory TRMs the specimens were heated to 610 °C in a vacuum (1–10 Pa), held at that temperature for 45 (for the first TRM acquisition, TRM1) and 60 min (for the second TRM acquisition, TRM2), and then cooled to the room temperature
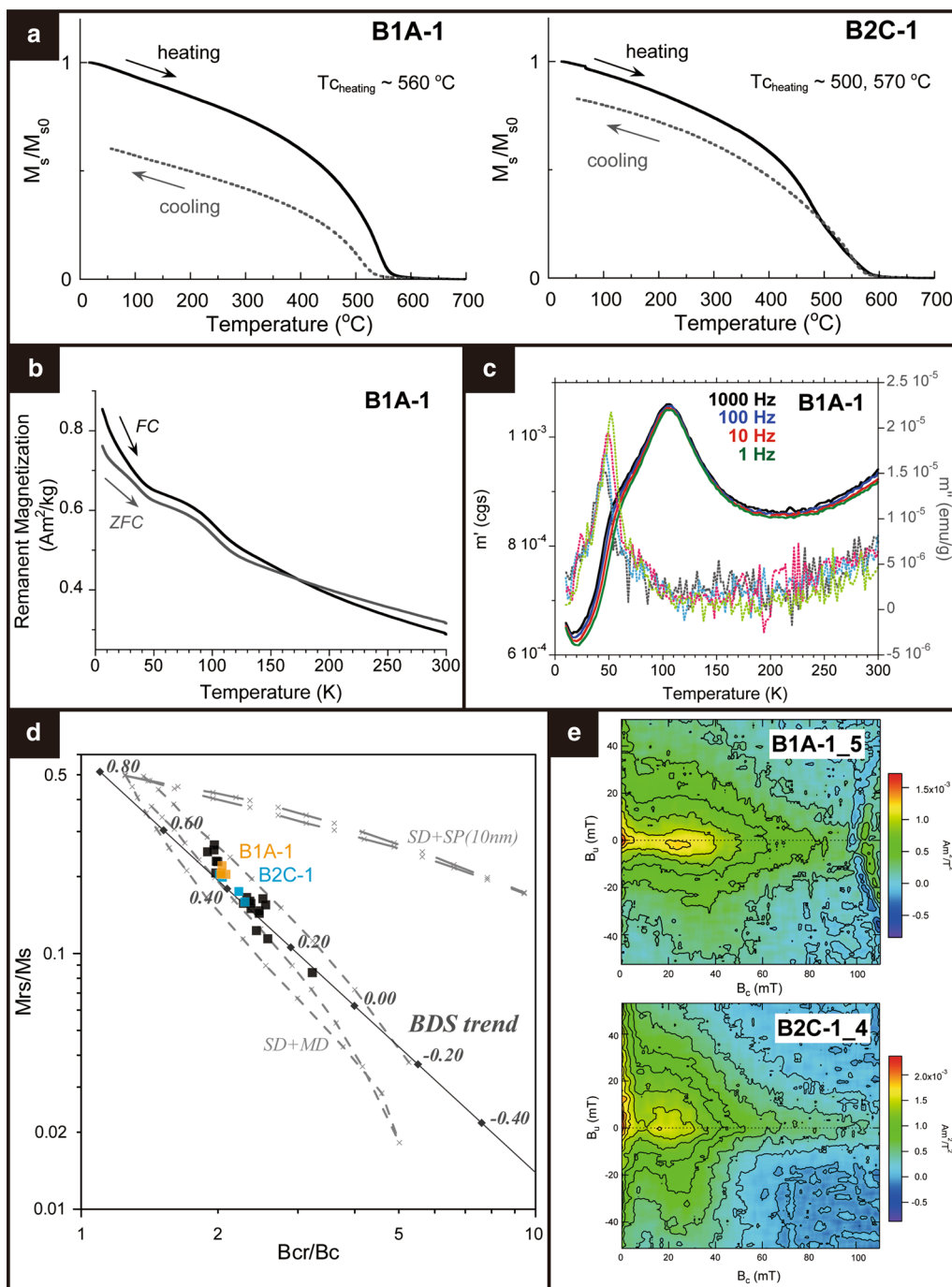
Fig. 2 Summary of rock magnetic results. **a** High-temperature strong-field thermomagnetic curves between the room temperature and 700 °C on two subsamples (B1A-1 and B2C-1). Solid (dotted) line shows heating (cooling) curve. **b** Low-temperature heating curves of ZFC and FC remanences from 10 to 300 K on a subsample B1A-1. **c** Low-temperature low-field thermomagnetic curves (only heating curves) of the in-phase magnetic susceptibility (m′) and the out-of-phase susceptibility (m″) with different frequencies on a subsample B1A-1. **d** Mrs/Ms versus Bcr/Bc diagram for the studied samples (square symbols) yielding an acceptable Tsunakawa–Shaw API estimate (see Table 2), with the theoretical curves for mixtures of SD and MD particles (three dashed lines), for the mixtures of SD and SP (10 nm in size) particles (two long-dashed lines) by Dunlop (2002a, b), and the BDS trend line (solid line) with labels of some BDS values (diamond symbols) by Paterson et al. (2017). **e** FORC diagrams for two subsamples B1A-1_5 and B2C-1_4 with a smoothing factor = 10

for ~3 h, using a TDS-1 thermal demagnetizer with a built-in DC field coil (Natsuhara Giken). The set DC field was variable between 15 and 30 µT. Before starting progressive AFD treatment of remanent magnetization, LTD was conducted as described in "Paleomagnetic direction analyses" section.

The experimental result for each specimen was plotted on NRM versus TRM1* and TRM1 versus TRM2* diagrams, where TRM1* and TRM2* are the corrected TRMs using the ARM correction technique of Rolph and Shaw (1985) in the first and second heating, respectively, expressed as TRM1* = TRM1 × ARM0/ARM1 and TRM2* = TRM2 × ARM1/ARM2, where TRM1, TRM2, ARM0, ARM1, and ARM2 are the remanence intensities at each AF step.

An API value was estimated by determining the slope of the linear segment defined for the NRM-TRM1* diagram when the ARM correction was validated by the slope of unity of the linear segment of the TRM1–TRM2* diagram. Each API estimate was judged by a set of the following selection criteria, which are similar to those adopted in the recent TS-based paleointensity studies (Yamamoto et al. 2010, 2015; Yamazaki and Yamamoto 2014; Ahn et al. 2016):

1. A primary NRM component should be isolated by progressive AFD on the Zijderveld diagram.
2. On the NRM-ARM1* diagram, a single linear segment for the slope calculation should be recognized within the coercivity range defining the primary NRM component. The segment should have at least 30% of the total extrapolated NRM intensity [$f_N \geq 0.30$, where the definition of f_N is equivalent to that designed by Coe et al. (1978)]. Its correlation coefficient should not be less than 0.995 ($r_N \geq 0.995$).
3. On the TRM1-TRM2* diagram, a single linear segment should also be recognized with $f_T \geq 0.30$ and $r_T \geq 0.995$. Its slope is unity within experimental errors with $1.05 \geq slope_T \geq 0.95$, as proof of the validity of the ARM correction.

IZZI-Thellier (IZZI-T) method with pTRM checks

For eight selective cylindrical specimens (six for site B1 and 2 specimens for site B2), the IZZI-T PI experiments with pTRM checks were performed. The peak temperatures of heating steps set in this study were, in addition to the room temperature, 150, 225, 300, 335, 370, 400, 435, 470, 500, 520 (or 525), 545 (or 550), 570 (or 575), and 600 °C. All heating–cooling procedures were performed in air using a TDS-1 thermal demagnetizer equipped with a built-in fan (Natsuhara Giken). Remanence measurements were made using a SMD-88 spinner

magnetometer (Natsuhara Giken) at the room temperature and after every heating–cooling treatment. At each temperature step, the specimen was heated to that temperature, maintained for 25 min, and then cooled to the room temperature using the built-in fan, both in the presence (in-field step) and absence (zero-field step) of a laboratory field ($F_{lab} = 15$ µT, which was directed along the y-axis ($+y$) of the specimen, for this study). Note that the laboratory field, 15 µT, is for minimizing the difference in intensity with the field in which the NRM was acquired, based on the TS results later described in "API determination" section, because of the adverse effect on the Arai diagram as found by Shaar et al. (2011). The order of in-field and zero-field steps was alternated at each temperature step [in-field-zero-field (IZ) versus zero-field-in-field (ZI)]. The pTRM check steps were inserted between every ZI step.

Each specimen-level experimental result was analyzed in the Arai diagram using the Thellier GUI program included in the PmagPy software package (Shaar and Tauxe 2013; Tauxe et al. 2016). To evaluate API determination on each specimen-level result using the conventional best-fitting line procedure, we used the following statistics: n, n_{pTRM}, DRATS, SCAT, FRAC, Gap Max, Beta (β), MAD$_{free}$, DANG, k'. Definitions of each statistic can be found in Paterson et al. (2014) as well as Cromwell et al. (2015), and brief descriptions of these statistics are as follows:

n: the number of points on an Arai diagram used to estimate the best-fit linear segment (the PI),

n_{pTRM}: the number of pTRM checks used to estimate the best-fit segment on an Arai diagram,

DRATS (Tauxe and Staudigel 2004): the sum of the difference between the original pTRM at a given temperature step and the pTRM check, normalized by the pTRM gained at the maximum temperature used for the best-fit on the Arai diagram,

SCAT (Shaar and Tauxe 2013): a Boolean statistic that uses the error on the best-fit Arai diagram slope to test the degree of scatter over a range of NRM/TRM data points,

FRAC (Shaar and Tauxe 2013): a measure of the NRM fraction of a selected range of NRM/TRM data points on an Arai diagram, based on the vector difference sum calculation,

Gap Max (Shaar and Tauxe 2013): the maximum gap between two NRM/TRM data points determined by vector arithmetic,

Beta (β) (Coe et al. 1978; Tauxe and Staudigel 2004): a measure of the relative scatter around the best-fit line in an Arai diagram,

MAD$_{free}$ (Kirschvink 1980): maximum angular deviation of the free-floating directional fits to the

paleomagnetic vector in selected NRM steps on a vector component diagram,

DANG (Tanaka and Kobayashi 2003; Tauxe and Staudigel 2004): the angular difference between the free-floating best-fit vector and the direction passing by the data center of a mass and the origin for selected NRM data points on a vector component diagram,

k' (Paterson 2011; Paterson et al. 2015): a measure of the degree of curvature between a selected range of the data points in an Arai diagram.

Our bundle of the statistics were mainly based on those documented by Cromwell et al. (2015), and adopted their threshold values as a selection criteria for evaluation (the so-called CCRIT selection criteria) with minor modifications that involve threshold values of three additional statistics, n and n_{pTRM}, and DRATS (as its threshold value, adopted that in Donadini et al. 2011; Sprain et al. 2016, etc.) that replace SCAT (not used in evaluating our API results). Our adopted threshold values of the statistics are as described below:

$n \geq 4$, $n_{\mathrm{pTRM}} \geq 2$, FRAC ≥ 0.78, Gap Max ≤ 0.60, $\beta \leq 0.10$, $\mathrm{MAD_{free}} \leq 5.0°$, DANG $\leq 10.0°$, $|k'| \leq 0.164$, and DRATS $\leq 22.0°$.

Results and discussion

Rock magnetic signature

Representative results of rock magnetic measurements are summarized in Fig. 2.

Figure 2a shows results of the in-air high-temperature thermomagnetic curves on representative subsamples. The curves are slightly different between sites but share a common characteristic that has a Curie temperature (T_c) between 560 and 570 °C during the heating curve and reduction in magnetization intensity at the cooling curve after heating. This is suggestive of the presence of nearly pure magnetite or Ti-poor titanomagnetite (presumably $x < 0.1$ for the $\mathrm{Fe_{3-x}Ti_xO_4}$ formula) in the natural samples and possible occurrence of oxidation of (titano-)magnetite to (titano-)hematite during the laboratory heating.

Low-temperature thermomagnetic curves of FC and ZFC remanences and of magnetic susceptibilities ($m = m' - i\,m''$, where m' and m'' are the in-phase magnetic susceptibility and the out-of-phase susceptibility, respectively) with different frequencies on a representative subsample, respectively, are shown in Fig. 2b, c. The curves of FC/ZFC remanence and susceptibility show, respectively, a broad but marked intensity transition at around 100–120 K and a peak in m' and minimum in m'' at ~110 K; this is considered to be related to the Verwey transition temperature for Ti-poor titanomagnetite (Özdemir et al. 1993; Moskowitz et al. 1998), existence of which is obviously supported by the T_c determined from the high-temperature curves. In addition, there

also appears to be a transition in FC/ZFC remanence and a maximum in m'' at around 40–50 K for both of the low-temperature thermomagnetometry. In this study the source of the ~40–50 K transition cannot be well constrained. Several candidate magnetic minerals for the source are possible: a rhombohedral phase of Fe–Ti oxide (Ishikawa et al. 1985), an antiferromagnetic mineral such as ilmenite (Moskowitz et al. 1998), magnetite (Moskowitz et al. 1998; Skumryev et al. 1999), or partially oxidized magnetite (Özdemir et al. 1993). The former two candidates have no remanent magnetization at the room temperature.

Magnetic hysteresis parameters on an Mrs/Ms versus Bcr/Bc diagram (Day et al. 1977) and FORC analysis provide information about grain size and magnetic interactions of the contained magnetic minerals. Our hysteresis parameters data in the Day diagram lie on the SD-MD mixing curves (Fig. 2d). The observed FORC diagrams are represented by two intensity peaks around 20–30 mT and near-zero mT on the Bc axis and some spreading of contours in the Bu-axis-direction (Fig. 2e). Furthermore, the slightly larger remanence intensity in FC than ZFC (Fig. 2b) is analogous to the FC/ZFC curves for sample 3006, which has a nominal grain size of 2–3 μm corresponding to PSD sizes, documented in Kosterov (2003). These infer mixtures of magnetostatically interacting large SD (or PSD-like) and MD particles in our samples.

In addition, ratios of the hysteresis parameters Mrs/Ms and Bcr/Bc allow us to calculate the bulk domain stability (BDS), which is suggested by Paterson et al. (2017) and is a quantitative parameter representing the degree of capability in maintaining stable remanence, also associated with content of MD particles (see Paterson et al. (2017) for BDS calculation, where BDS value is 1 when a single grain yields a perfectly square hysteron). BDS values of our analyzed samples range between 0.12 and 0.52 (see Fig. 2d), where Paterson et al. (2017) described the BDS threshold of > 0.1 as a first-order threshold, aimed at screening out samples that will not be useful in the API experiments.

Paleomagnetic direction

A total of 11 specimens for 2 sites were analyzed to isolate the characteristic remanent magnetization (ChRM) of each from progressive AF demagnetization with pre-LTD-treatment. All the specimens, except specimen B1D-2-1, revealed similar directions after demagnetization by ~10–20 mT (see Fig. 3a). Specimen B1D-2-1 exhibited an anomalous direction in high demagnetization steps. This could arise from misorientation in specimen preparation. Through PCA, a stable ChRM direction was well defined with $\mathrm{MAD_{free}} < 8°$ for each specimen, except for one (B2B-2-1), which exhibited a
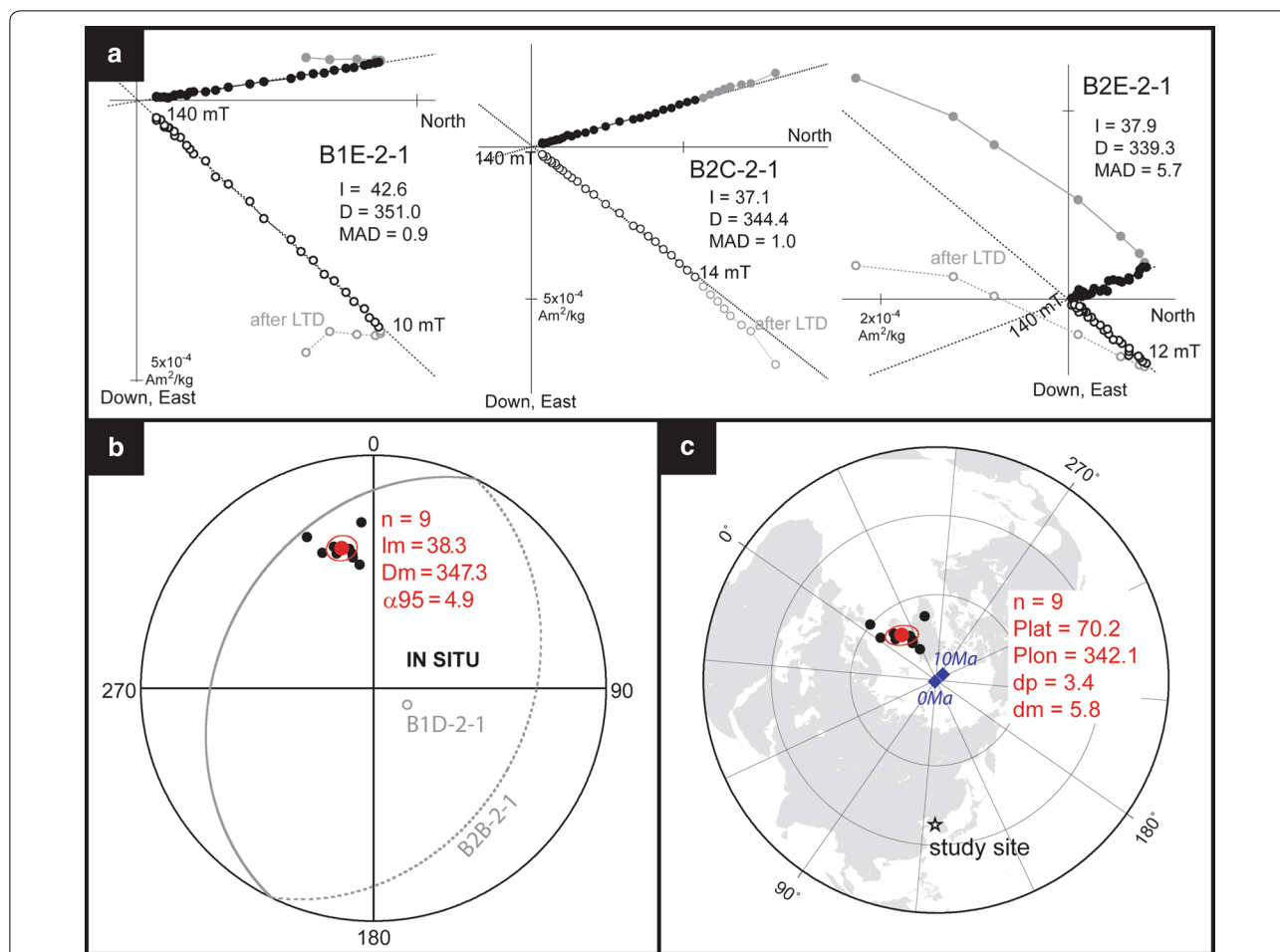
Fig. 3 Summary of paleodirectional results. **a** Examples of progressive AFD (with the LTD pre-treatment) results of NRMs displayed on Zijderveld diagrams with geographic coordinate system. Determination of a ChRM direction from the PCA (Kirschvink 1980) is shown in each Zijderveld diagram. **b** Equal-area projection of ChRM directions from 11 specimens for two sites, with an overall mean of the ChRMs and its 95% confidence limit (shown in red). Grey-colored data represent data excluded in calculating the overall mean. Note that, for specimen B2B-2-1, a great circle fit by the technique of Halls (1976, 1978) is shown. **c** VGP positions calculated from the ChRM direction data used in the ChRM mean determination (see Fig. 3b) on the northern hemisphere, with their mean and the corresponding 95% confidence limit (shown in red). For reference, synthetic poles for East Asia at 0 and 10 Ma suggested by Cogné et al. (2013) are shown as diamonds. Location of the studied area is shown as a star

strong overprint of secondary remanence of reverse-magnetized. Hence, individual site-mean ChRM directions for the two sites could be calculated as listed in Table 1. These two site-mean directions are close to and statistically indistinguishable from each other, thereby allowing us to obtain an in situ overall mean of $D = 347.3°$ and $I = 38.3°$ with $\alpha_{95} = 4.9°$ and $k = 113.4$ ($n = 9$) (see also Fig. 3b).

The overall mean is obviously different from both the present field direction ($D = \sim 352°$, $I = \sim 55°$; IGRF-12, Thébault et al. 2015) and the expected geocentric axial dipole (GAD) direction at the studied geographic location ($D = 0°$, $I = \sim 57°$). The corresponding virtual geomagnetic pole (VGP) is at 342.1° in longitude and

Table 1 Mean ChRM directions for sites

Site	n/N	Dm	Im	α95	k
B1	4/5	352.8	39.2	8.4	119.6
B2	5/6	343.0	37.3	6.0	164.4
B1 + B2	9/11	347.3	38.3	4.9	113.4

n/N, the number of specimen-level ChRM determinations used in mean calculation/the number of specimens measured; Dm (Im), declination (inclination) of mean ChRM determination; *a*95, 95% confidence limit; and *k*, precision parameter

70.2° in latitude (with dp = 3.4° and dm = 5.8°) (Fig. 3c), which is ~ 20° from both the geographic North Pole and the reference pole for East Asia at ~ 5 Ma from Cogné

et al. (2013). These results probably originate from an instantaneous feature of the Jinchon Basalt: timing of the emplacement and cooling cannot be known exactly but is presumed as being geologically short, insufficient to average out the paleomagnetic secular variation during a period of normal polarity.

API determination

Tsunakawa–Shaw (TS) determination

For specimens subjected to the TS method, about 11–24% of ARM0 intensity was demagnetized by LTD (see LTD_{A00} values in Table 2), suggestive of the relatively large contribution of the remanence component carried by MD particles.

Examples of the TS API results for two specimens (B1A-1-1 and B2C-1-1) meeting our set of criteria (see "Tsunakawa–Shaw (TS) method" section) are shown in Fig. 4a. In each of the NRM-TRM1* diagrams a linear segment cloud be defined after AF demagnetizations by 8–22 mT (soft), in which the MD-carried remanence component could be erased. The individual determined linear segment has a large portion ($f_N > 0.7$) and high value in the correlation coefficients ($r_N \geq 0.998$).

Non-ideal results that could not meet the specimen-level selection criteria, such as in Fig. 4b (an example of specimen B2B-1-1), all fail by reason of low correlation coefficient values in the NRM-TRM1* diagrams ($r_N < 0.995$) and non-unity of the slope in the TRM1-TRM2* diagrams ($slope_T > 1.05$). It is also found that these failed results have a large portion of unusual overprint of remanence in low-coercivity spectra on the individual orthogonal diagrams of the NRM demagnetization result.

The TS experiments yield 13 (out of 21) specimen-level API estimates that meet our set of criteria (Table 2). The acquisition rate of the acceptable API estimates is 62%. All of the specimen-level acceptable estimates, with one exception (specimen B2F-1-1, 3.3 µT), yield values in range between 11.3 and 15.9 µT, which represent remarkably low values compared to the present-day intensity at the site location (~ 52 µT). These allow two mean API values, 12.6 µT (± 1.2 µT, standard deviation; $N=10$) and 15.9 µT (± 0.1 µT; $N=2$ when discarding the B2F-1-1 estimate in calculation) for the B1 and B2 site, respectively (Table 2). Since, despite of the somewhat difference of site means between them, both indicates low estimates, we combine the 12 specimen-level estimates of both sites, excluding the B2F-1-1 estimate (3.3 µT), and obtain an overall mean of 13.1 µT with a standard deviation of 1.7 µT (13% of the mean).

We also obtain similar API estimates from all pairs of companion specimens that were set to different B_{lab} values in the experimental condition (see Table 2). It is also

found that there is a consistency in the API estimates even for samples with variability in the average size of contained magnetic particles (for example, the BDS values ranging from ~ 0.3 to ~ 0.5 as shown in Fig. 2d). The independence of the API estimates from both the B_{lab} value and the magnetic stability suggests high-fidelity API estimates by the TS method.

IZZI-Thellier (IZZI-T) determination

Eight specimens from six samples (five for B1 site and one for B2 site) were subjected to the IZZI-T API experiments. Examples of the IZZI-T results are shown in Fig. 5. NRM/TRM data points in the Arai diagram appear to fall onto a curved or kinked line, leading to a failure to determine a characteristic straight line in which the slope was utilized in the API calculation. All the Arai diagrams analyzed reveal such problematic patterns for API determination; this is not surprising because there are certainly contributions from MD remanences in the samples, as suggested from the LT-demagnetized components in ARMs and the FORC diagrams. The degree of the curvature vary by sample (the k values given in Table 3). NRM directions for the zero-field steps appear to be similar after 225 °C but the direction becomes closer to the laboratory field directions as the temperature step increases. These characteristic observations are likely to be responsible for the effect of the MD particles. The pTRM checks are still positive at 500 °C or higher, although the pTRM check at 550 °C appears to be inconclusive or negative.

Due to their curved signature patterns, each of the analyzed Arai diagrams can take variable slope values corresponding to (not actual) API estimates spanning mostly from ~ 3 to > 30 µT. Examples of API determinations by the conventional best-fitting line technique for the individual diagrams are given in Table 3. In all analyzed specimens, there are no API determinations meeting our criteria. Thus, it is concluded that the best-fitting line technique for our IZZI-T results cannot give meaningful API estimates.

The cause of the curved (or two-slope) Arai diagrams is hard to be clarified in this study but it is possibly considered to be dominantly related to the presence of MD particles (see, e.g. Levi 1977; Fabian 2001; Coe et al. 2004; Leonhardt et al. 2004; Xu and Dunlop 2004; Shaar et al. 2011; Paterson et al. 2015), which was suggested by the results of the hysteresis parameters and FORC diagrams (as documented in "Rock magnetic signature" section) and the intensity decay of remanences by LTD (see "Tsunakawa–Shaw (TS) determination" section). The occurrence of MD particles can be also supported by the "zigzagged" pattern, being superimposed on the curved Arai diagram, as seen in Fig. 5 (Tauxe and Staudigel

Table 2 Summary of results of the Tsunakawa–Shaw API experiments

Specimen	$NRM_{LTD,0}$ (Am^2/kg)	$ARM0_0$ (Am^2/kg)	MDF_{A0} (mT)	LTD_{A00} (%)	NRM H_L (mT)	NRM H_H (mT)	D (°)	I (°)	MAD_{free} (°)	First heating H_L (mT)	First heating H_H (mT)	$Slope_{A0}$	$Slope_N$	f_N	r_N	Second heating H_L (mT)	Second heating H_H (mT)	$Slope_{A1}$	$Slope_T$	f_T	r_T	B_{lab} (µT)	B_{anc} (µT)
B1A-1-1	8.63E−04	1.17E−03	28	17	8	180	nd	nd	1.6	8	180	0.936	0.397	0.926	0.998	0	180	0.993	0.976	0.989	1.000	30.0	11.9
B1A-2-1	9.51E−04	1.11E−03	27	19	18	140	350.1	39.2	0.9	18	60	0.841	0.591	0.596	0.999	0	180	0.991	0.989	0.991	1.000	20.0	11.8
B1B-1-1	9.80E−04	1.41E−03	31	14	4	180	nd	nd	1.0	4	180	0.942	0.385	0.969	0.997	0	180	0.999	1.029	0.989	0.999	30.0	11.6
B1B-2-1	8.66E−04	1.27E−03	30	13	2	140	353.7	45.7	1.1	2	140	0.909	0.566	0.986	0.997	0	180	1.013	0.988	0.989	1.000	20.0	11.3
B1D-1-1	7.11E−04	8.90E−04	25	24	20	180	nd	nd	2.3	20	180	0.829	0.977	0.624	0.995	0	180	0.989	1.000	0.985	0.999	15.0	14.7
B1D-2-1	8.00E−04	8.93E−04	26	23	10	140	115.6	−77.0	1.2	10	140	0.852	0.665	0.896	0.998	0	180	1.013	0.973	0.990	1.000	20.0	13.3
B1E-1-1	9.08E−04	9.52E−04	29	20	10	180	nd	nd	1.0	10	180	0.869	0.861	0.928	0.998	0	180	0.987	1.003	0.993	1.000	15.0	12.9
B1E-2-1	5.42E−04	8.72E−04	28	21	10	140	351.0	42.6	0.9	10	140	0.842	0.589	0.902	0.998	0	180	1.004	0.990	0.989	1.000	20.0	11.8
B1G-1-1	8.53E−04	1.04E−03	28	20	10	180	nd	nd	1.4	10	180	0.878	0.947	0.902	0.996	0	180	0.998	1.005	0.989	1.000	15.0	14.2
B1G-2-1	6.59E−04	1.03E−03	28	21	10	140	355.9	29.3	0.9	10	140	0.902	0.611	0.883	0.996	0	180	0.981	1.021	0.988	1.000	20.0	12.2
B2B-1-1	3.79E−04	1.60E−03	29	21	20	180	nd	nd	7.5	20	180	0.791	0.210	0.655	**0.985**	0	180	0.982	**1.136**	0.977	0.999	15.0	nd
B2B-2-1	5.96E−04	1.57E−03	23	20	22	140	nd	nd	8.2	22	140	0.724	0.179	0.599	**0.991**	0	180	1.000	**1.130**	0.974	0.999	20.0	nd
B2C-1-1	9.65E−04	1.63E−03	31	11	22	180	nd	nd	1.7	22	180	0.753	1.055	0.721	0.998	0	180	0.978	1.027	0.985	0.999	15.0	15.8
B2C-2-1	9.64E−04	9.64E−04	28	13	14	140	344.4	37.1	1.0	14	140	0.813	0.797	0.884	0.999	0	180	0.973	1.023	0.990	0.999	20.0	15.9
B2D-2-1	1.70E−04	1.38E−03	26	23	10	140	336.3	29.9	3.6	10	140	0.578	0.222	0.907	**0.979**	0	180	0.996	**1.091**	0.983	1.000	20.0	nd
B2E-1-1	3.79E−04	1.53E−03	25	23	16	180	nd	nd	6.1	16	180	0.562	0.239	0.669	**0.988**	0	180	0.994	**1.075**	0.970	0.999	15.0	nd
B2E-2-1	2.31E−04	1.38E−03	20	24	12	140	339.3	37.9	5.5	12	140	0.527	0.168	0.701	**0.978**	0	180	1.002	**1.069**	0.975	0.999	20.0	nd
B2F-1-1	3.11E−04	1.56E−03	23	16	14	180	nd	nd	6.2	14	180	0.560	0.219	0.644	0.995	2	180	1.016	1.038	0.978	0.999	15.0	3.29
B2F-2-1	2.87E−04	1.40E−03	19	22	20	140	344.8	39.9	5.1	20	140	0.525	0.179	0.587	**0.989**	0	180	0.993	1.041	0.980	0.999	20.0	nd
B2G-1-1	5.31E−04	1.44E−03	30	23	12	180	nd	nd	4.5	12	180	0.619	0.359	0.918	**0.976**	0	180	0.987	**1.131**	0.973	0.999	15.0	nd
B2G-2-1	4.36E−04	1.39E−03	24	23	20	140	351.1	41.3	5.9	20	140	0.623	0.203	0.602	0.996	0	180	0.984	**1.139**	0.983	1.000	20.0	nd

	N	Mean ± SD (µT)
B1 site mean	10	12.6 ± 1.2
B2 site mean	3	11.7 ± 7.3
B2 site mean#	2	15.9 ± 0.1
Overall mean	13	12.4 ± 3.2
Overall mean#	12	13.1 ± 1.7

$NRM_{LTD,0}$ intensity after LTD for NRM. $ARM0_0$ intensity after LTD for ARM0. MDF_{A0} median destructive field of ARM0. LTD_{A00} LT demagnetized fraction of ARM0, expressed as (ARM0 intensity after LTD)/(ARM0 intensity before LTD) × 100. H_L, H_H low (high) limit of the interval of AF steps chosen for the determination of a characteristic direction or a linear segment. D, I, MAD_{free} declination and inclination in the geographic coordinate system and the maximum angular deviation determined by the PCA free-floating fit (Kirschvink 1980) for the chosen intervals of data. Time, hold time at the set peak temperature (610 °C) in each heating process. The $slope_{A0}$, $slope_{A1}$, and slope values determined from all data points after LTD in each of the ARM0–ARM1 and ARM1–ARM2 diagrams. The $slope_N$, $slope_T$, slope values of the chosen linear segment in each of the NRM–TRM1* and TRM1–TRM2* diagrams. The f_N, f_T, NRM, and TRM1 fractions of the chosen linear NRM–TRM1* and TRM1–TRM2* segments. The r_N, r_T, correlation coefficients for linearity of the chosen linear segment of NRM/TRM1* and TRM1/TRM2* data points, respectively. B_{lab} laboratory DC field during the TRM1 and TRM2 acquisitions. B_{anc}, API estimate

"nd" denotes "not determined". Arabic numerals with bold italic denote the values failing to meet the corresponding selection criterion. In the bottom of the table, site means and overall means of API estimates are listed

The mean value with # mark is calculated from all other specimen-level estimates excluding one for specimen B2F-1-1 (3.29 µT)
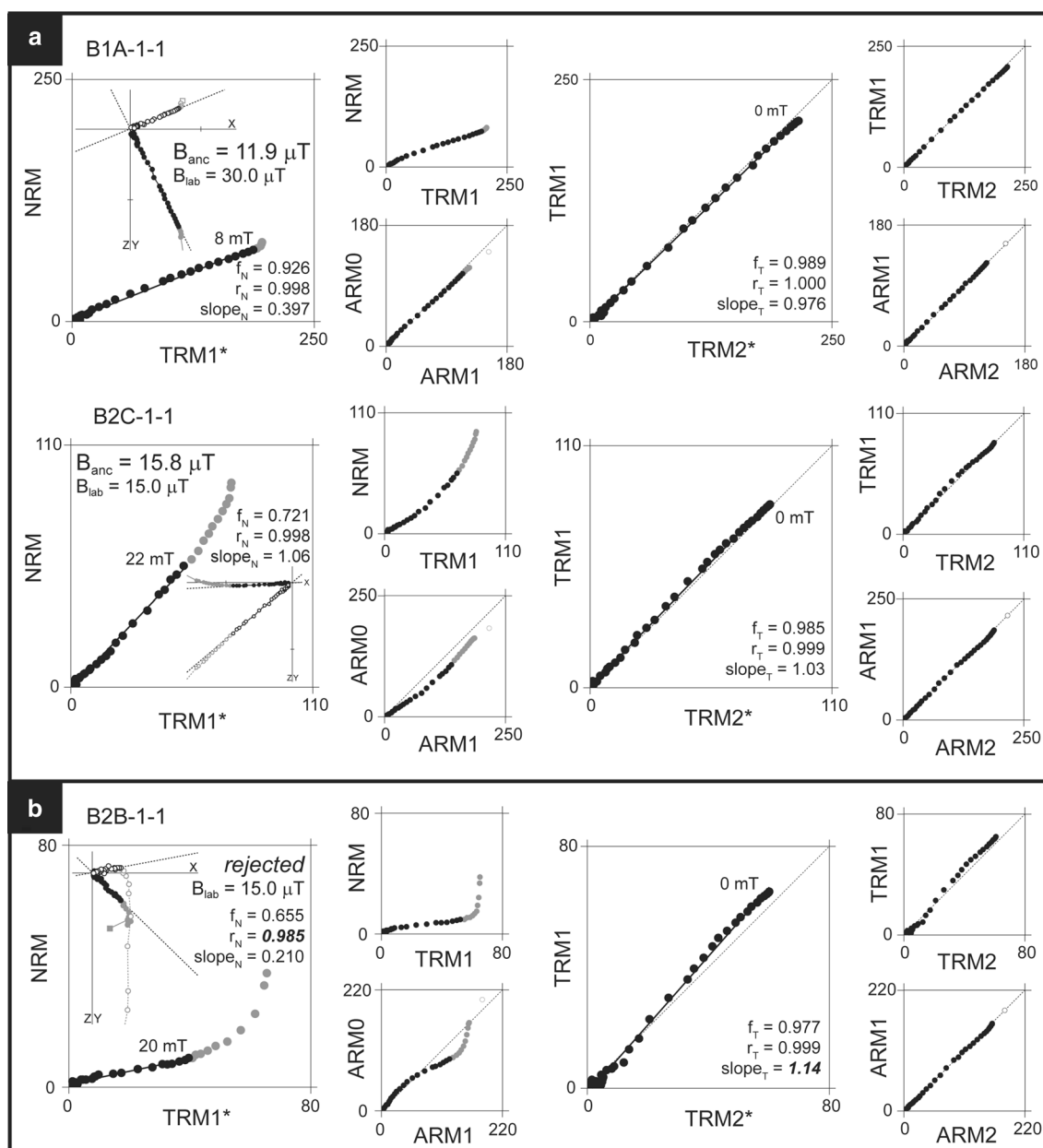
Fig. 4 Examples of results of the Tsunakawa–Shaw API experiments. **a** Two specimen-level successful results in API determination. **b** A failed result. Three diagrams shown on the left-hand (right-hand) side are from a pair of the prior (first) laboratory heating and the first (second) laboratory heating procedures, where black symbols show selected intervals of data for determining the linear segments. Inset of a Zijderveld diagram on each NRM versus TRM1* diagram shows the AF demagnetization result of NRM, where filled (open) symbols indicate projection onto the horizontal (vertical) plane

2004; Yu et al. 2004; Yu and Tauxe 2005). On the other hand, considering the rock magnetic signatures of the samples in more, magnetic interaction between the particles (e.g. Mankinen and Champion 1993) and/or thermal alteration of pre-existing magnetic minerals during the experiment (e.g. Mochizuki et al. 2004) might be also another possible cause for them. However, the magnetic interactions seem to be not the case for this as Coe 1974 and Fabian 2001 found that an average magnetostatic interaction of the particles is not likely to influence the shape of the Arai diagram noticeably. Mochizuki et al. (2004) reported, for PSD-like Ti-poor and Ti–rich titanomagnetites-bearing samples of the Oshima 1986 lava, two-slope Arai patterns on the Coe's version Thellier
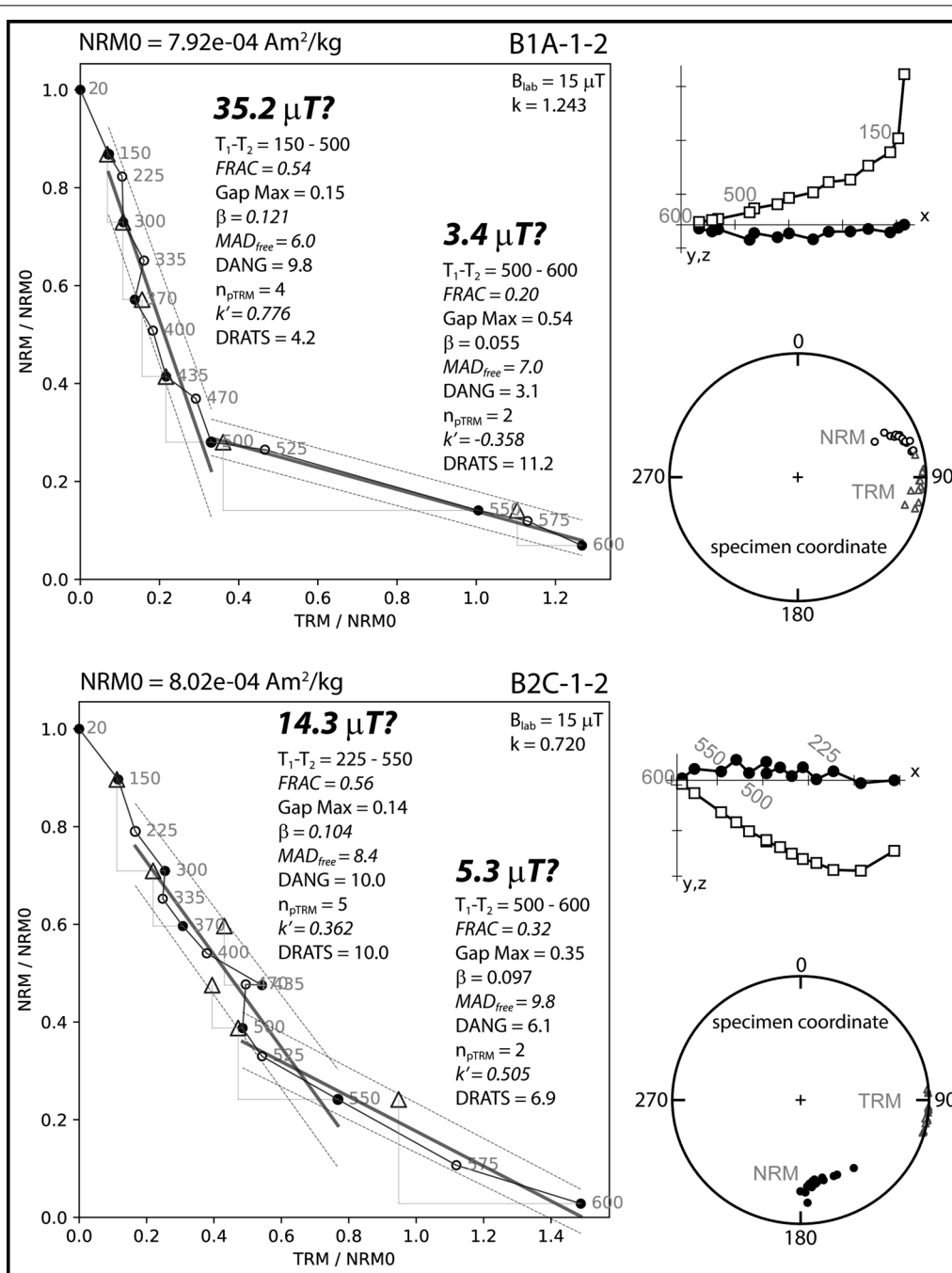
Fig. 5 Two examples of results of the IZZI-Thellier API experiments. For each example, the Arai diagram (left-hand), the orthogonal projection of the zero-field steps (NRMs) (upper right-hand), and the equal-area projection of NRMs and laboratory-induced TRMs in the specimen coordinate systems (lower right-hand) are shown. In each Arai diagram, filled (open) circles represent the ZI (IZ) steps, triangles are the pTRM checks, and each green line and the two neighboring dotted lines are the best-fit lines for each of the selected temperature steps and the associated threshold lines that define boundaries for the SCAT statistics (see Shaar and Tauxe 2013 for details). The Arai diagrams show curved (or kinked) patterns with different degrees of the curvature ($k = 1.243$ and $k = 0.720$, respectively), resulting in obtaining no qualified API estimate when applying the conventional best-fitting line technique. For each Arai diagram two examples of the best-fitting line are shown with the associated statistical values (see text for details). For the orthogonal projection, filled circles (open squares) show projections of data at temperature steps on the y–x (z–x) plane and the x-axis is rotated to the horizontal direction of the initial NRM. For the equal-area projection, circles (triangles) represent NRM (TRM) data at temperature steps and filled (open) symbols represent projection of data on the lower (upper) hemisphere

Table 3 Summary of results of the IZZI-Thellier API experiments with the conventional best-fitting line interpretations

Specimen	NRM0 (Am²/kg)	B_{lab} (μT)	θ	k	$T_1 - T_2$ (°C)	n ≥4	FRAC ≥0.78	Gap Max ≤0.60	β ≤0.100	MAD_{free} (°) ≤5.0	DANG (°) ≤10.0	n_{pTRM} ≥2	DRATS ≤22	SCAT	k' |k'| ≤0.164	B_{anc} (μT)*
B1A-1-2	7.92E−04	15.0	28	1.243	150–600	13	0.74	0.14	0.165	5.5	6.8	6	11.2	Fail	1.273	9.5?
					150–500	9	0.54	0.15	0.121	6.0	9.8	4	4.2	Fail	0.776	35.2?
					500–600	5	0.20	0.54	0.055	7.0	3.1	2	11.2	Pass	−0.358	3.4?
B1B-1-2	1.05E−03	15.0	34	1.167	150–600	13	0.82	0.14	0.149	4.7	5.0	6	2.5	Fail	1.188	9.2?
					150–500	9	0.57	0.17	0.090	5.0	5.8	4	0.5	Fail	0.531	29.2?
					500–600	5	0.25	0.48	0.084	11.1	2.0	2	2.5	Pass	−0.577	3.4?
B1B-2-2	9.53E−04	15.0	54	1.191	225–600	12	0.70	0.14	0.163	5.3	5.9	6	17.6	Fail	1.217	9.0?
					225–500	8	0.48	0.17	0.116	5.5	6.1	4	1.9	Fail	0.600	27.7?
					500–600	5	0.22	0.44	0.125	13.4	3.9	2	17.6	Pass	0.000	3.3?
B1D-1-2	9.47E−04	15.0	99	1.123	150–600	13	0.79	0.14	0.149	4.8	7.6	6	18.5	Fail	1.162	12.2?
					150–520	10	0.60	0.19	0.091	4.8	10.3	4	7.5	Pass	0.507	31.8?
					520–600	4	0.20	0.36	0.034	11.8	2.7	2	18.5	Fail	−0.144	4.0?
B1E-1-2	8.49E−04	15.0	70	1.142	150–600	13	0.75	0.12	0.144	4.9	7.7	6	20.4	Fail	1.165	11.5?
					150–500	9	0.49	0.18	0.044	5.0	8.2	4	1.1	Pass	0.279	33.3?
					500–600	5	0.26	0.32	0.109	14.1	7.4	2	20.4	Pass	0.566	4.4?
B1G-1-2	9.00E−04	15.0	50	1.163	0–600	14	0.94	0.11	0.152	5.1	7.6	6	18.0	Fail	1.163	11.9?
					0–500	10	0.66	0.16	0.051	4.4	8.8	4	2.2	Pass	0.235	32.7?
					500–600	5	0.28	0.32	0.124	16.3	3.4	2	18.0	Pass	0.332	3.7?
B2C-1-2	8.02E−04	15.0	84	0.720	225–600	12	0.74	0.15	0.109	7.0	6.4	6	6.9	Fail	0.740	9.1?
					225–550	10	0.56	0.14	0.104	8.4	10.0	5	10.0	Pass	0.362	14.3?
					500–600	5	0.32	0.35	0.097	9.8	6.1	2	6.9	Pass	0.505	5.3?
B2C-2-2	1.29E−03	15.0	43	0.993	150–600	13	0.75	0.17	0.138	8.3	8.7	6	7.4	Fail	0.958	11.9?
					0–520	11	0.77	0.31	0.115	5.1	15.9	4	20.6	Fail	0.681	30.6?
					500–600	5	0.25	0.38	0.078	5.1	3.0	2	7.4	Pass	0.441	5.9?

All of the analyzed specimens have no API estimate that meet our optimized selection criteria but some of the interpretations for specimens are shown. NRM0, initial NRM intensity. B_{lab}, laboratory DC field during TRM acquisitions (in-field steps). θ, the angle between directions of the field in which NRM of the sample was produced and B_{lab}. k, a measure of the curvature for all temperature steps (Paterson 2011). $T_1 - T_2$, temperature interval used in the determination. For the explanations of statistics of n, FRAC, Gap Max, b, MAD_{free}, DANG, n_{pTRM}, DRATS, SCAT and k', see "IZZI-Thellier (IZZI-T) method with pTRM checks" section. Note threshold values of the statistics for the selection criteria are documented under the column headings. B_{anc}*, the value of the determined slope of NRM/TRM data for the selected temperature steps in the Arai diagram multiplied by the B_{lab} value

Letters with italics denote the values failing to meet the corresponding selection criterion

experiments (Coe 1967) and change in the remanence directions at the zero-field steps converging towards the direction of the lab field above elevated temperatures. They attributed them to acquisition of chemical remanences by gradual thermal alteration of the contained magnetic minerals with intermediate degrees of high-temperature oxidation due to the laboratory heating during experiment. We consider this to be not the case for our Thellier results because our samples do not contain such Ti-rich titanomagnetites thereby being hard to follow the scenario possibility of the magneto-mineral change Mochizuki et al. (2004) suggested. The directional changes towards the lab field in this study is more likely caused by the portion of remanence acquired during the "in-field" step (the so-called "pTRM tails"), which is not fully removed in the subsequent "zero-field" step, as mentioned for the "MD" slag samples in Shaar et al. (2011).

Our IZZI-T results, alternatively, can be analyzed by a bootstrap technique in constraining the API estimate, in a similar way as described in Shaar et al. (2011), because the Arai diagram patterns are likely caused by the influence of partly contained MD particles as mentioned above. The bootstrap technique in this study were performed using a Microsoft Excel sheet and give a 95% confidence interval of API estimates as an overall mean of the specimen-level values, by applying the following procedure:

I. For the Arai diagram data of each specimen, all API values meeting a loose set of selection criteria ($n \geq 4$, $f \geq 0.3$, and $\beta \leq 0.2$; see Paterson et al. (2014) for definitions of the statistics) are determined and calculated using the auto interpreter in the Thellier GUI program. The minimum and maximum of the calculated API values for each Arai diagram result are denoted B_{min} and B_{max}, respectively.

II. By applying a second screening criteria of $B_{max}/B_{min} \geq 5$, the specimen-level results are selected for the next calculation.

III. For individual sets of values from the B_{min} to B_{max}, a re-sampling routine is run, using an Excel sheet, to pick values randomly and generate a large number of combinations ($n = 10,000$ for this study) of the picked values from individual specimen-level results meeting $B_{max}/B_{min} < 5$.

IV. From the 10,000 combinations, a total of 10,000 means are calculated and the 95% confidence interval of their probability distribution is provided as a constraint of mean API estimate we seek.

Results of the bootstrap procedure are summarized in Table 4. Six of the eight specimens exhibit results with B_{max}/B_{min} ratios of ten or higher, associated with large degrees of the curvature of the Arai diagram result (1.12 to 1.24 in k). Eventually, two specimen-level results (B2C-1-2 and B2C-2-2) that have k values less than 1.00 meet the $B_{max}/B_{min} < 5$ criterion and give us a bootstrap-derived 95% confidence interval of 6.6 to 19.7 µT as an estimation of the API at which the Jinchon Basalt was emplaced. It is also recognized that when the bootstrap

Table 4 Summary of API determination using a bootstrap approach (in a similar way to that documented in Shaar et al. 2011) for the IZZI-Thellier results

Specimen	NRM0 (Am²/kg)	B_{lab} (µT)	θ	k	BDS_m	Information of specimen-level paleointensity estimates		Bootstrap constraints of overall mean[a]		
						$B_{min}-B_{max}$ (µT)	B_{max}/B_{min}		95% confidence interval (µT)	Mean ± SD (µT)
B1A-1-2	7.92E−04	15.0	28	1.243	0.446	3.2–51.3	16	$N = 8$	9.9–24.0	16.6 ± 3.6
B1B-1-2	1.05E−03	15.0	34	1.167	0.467	3.1–39.9	13	$N = 2$	6.6–19.7	12.6 ± 3.5
B1B-2-2	9.53E−04	15.0	54	1.191	0.467	3.1–39.4	13	($B_{max}/B_{min} < 5$)		
B1D-1-2	9.47E−04	15.0	99	1.123	0.333	4.0–41.8	10			
B1E-1-2	8.49E−04	15.0	70	1.142	0.333	3.8–38.1	10			
B1G-1-2	9.00E−04	15.0	50	1.163	0.346	3.3–39.9	12			
B2C-1-2	8.02E−04	15.0	84	0.720	0.403	4.9–20.7	4.2			
B2C-2-2	1.29E−03	15.0	43	0.993	0.403	5.6–25.1	4.5			

NRM0, B_{lab}, θ, and k are the same as in Table 3. BDS_m, the associated mean value from the measurements of bulk domain stability (Paterson et al. 2017) by 4 subsamples for the drilled samples. B_{min}, B_{max}, the minimum and maximum of all of PI estimates that meet a loose set of selection criteria (n ≥ 4, f ≥ 0.3 and β ≤ 0.2; see Paterson et al. (2014) for definitions of the statistics) for each specimen

[a] Describes the information on an overall mean of API estimates obtained when running a re-sampling routine that randomly picks values from the B_{min} to B_{max} for each specimen and calculates a large number of their means (n = 10,000): N, the number of specimens used in the bootstrap procedure; S.D., the standard deviation of the 10,000 means. See "IZZI-Thellier (IZZI-T) determination" section for details

analysis is run without applying the B_{max}/B_{min} criteria, the resultant 95% confidence interval is between 9.9 and 24.0 μT, which is biased slightly high compared to that in which $B_{max}/B_{min} < 5$ although it is statistically indistinguishable. Given only the current observation, the necessity for the application of the B_{max}/B_{min} criterion in constraining an API estimate does not seem robust; this is an issue that needs to be checked further with a sufficient number of specimens.

There appears to be no clear relationship between the B_{max}/B_{min} ratio and the BDS value. The B2C sample, which includes the two B2C-1-2 and B2C-2-2 specimens with $B_{max}/B_{min} < 5$, has ~0.40 for the average BDS (BDS_m in Table 4); the other samples with $B_{max}/B_{min} > 5$ have ~0.33–0.47 for the average BDS (see Table 4). We postulate that the relationship might be possibly have been complicated by experimental conditions; for example, the ratio and the angle between the ancient field and the field applied during the Thellier API experiment, which are possible factors of the curvature in Arai diagram for non-SD materials (Biggin 2006; Paterson 2011; Shaar et al. 2011).

Average field intensity during the Early Pliocene

We found that, whether the B_{max}/B_{min} criterion was applied or not, the IZZI-T-derived confidence interval of average API, 6.6–19.7 μT or 9.9–24.0 μT, coincides reasonably with the TS-derived average of 13.1 ($\pm$1.7) μT. This concordance can support the feasibility of using the bootstrap approach in API determination of the Thellier experiments for non-SD-contained materials, as suggested initially by Shaar et al. (2011). We could assign, with high fidelity, the mean field intensity during the Jinchon Basalt emplacement as 13.1 μT; this is a remarkably low value compared to the present-day intensity at the site location (~52 μT) and an expected local intensity (~28 μT) under the GAD assumption with a VADM of 5×10^{22} Am^2.

Our new API data from Baengnyeong Island, despite a geologically short record of the geomagnetic field, provides an opportunity to discuss field behavior during the Early Pliocene, compared with the global API database, such as the PINT (Biggin et al. 2009, 2010). Figure 6a shows previously published data (grey crosses in the figure) of APIs as site/cooling unit-mean estimates for the age interval of 7 to 0.05 Ma, downloaded from the PINT database with version 2015.05 (http://earth.liv.ac.uk/pint/, accessed July, 2018), as a VADM versus age plot, where the VADM values were recalculated from this study using the individual sample latitudes because of mixing of VDM and VADM values and absence of VADM values in some downloaded data. In addition, 24 data points (mean estimates for

lava cooling units) reported in Ahn et al. (2016) are newly included in Fig. 6a. We note that these data in the PINT database have highly variable qualities associated with their reliabilities. To view after screening out low-quality data, we apply the quality criteria that each data point has the number used in the PI calculation of three or more ($N_F \geq 3$), a standard deviation of 20% or less ($\sigma_F \leq 20\%$), and stable polarity of normal or reverse (to omit "transitional" and "unknown" in the dataset), thereby extracting 614 data points fulfilling the quality criteria. Among the extracted data, we further extract only data that were determined by the TS method (LTD-DHT-S) and Thellier (or Thellier-modified) methods with pTRM checks ($T+$) including the correction technique by Valet et al. (1996) ($T + Tv$), shown as yellow circles (LTD-DHT-S; $n = 79$) and blue diamonds ($T+$ and $T + Tv$; $n = 368$) in Fig. 6a.

For the Early Pliocene there are only 23 data points from five studies (Bogue and Paul 1993; Laj et al. 2000; Goguitchaichvili et al. 2001; Tauxe et al. 2004; Yamamoto and Tsunakawa 2005) after the above data selection. The 23 data all were determined by the Thellier-type methods with pTRM checks ($T+$) or the Tsunakawa–Shaw method (LTD-DHT-S), and most of them are higher than 5×10^{22} Am^2 in VADM representing fairly high dipole strengths during the period compared to those of the past few Myr. Our low API estimate from Baengnyeong Island (Korea), using the inclination of our determined in situ ChRM mean and the site latitude, is calculated to be 2.87 (± 0.37) $\times 10^{22}$ Am^2 in VDM and 2.32 (± 0.30) $\times 10^{22}$ Am^2 in VADM (see also Fig. 6a), respectively. The new VADM data is the second smallest value for the period, inferring a possibility of more large variations in the dipole strength during the period.

Figure 6b shows quartile box plots of the selected VADMs including our new data for four geologic time spans, namely the Early Pliocene ($n = 24$), Late Pliocene ($n = 27$), Early Pleistocene ($n = 115$), and Middle-Late Pleistocene ($n = 269$), and Fig. 6c shows their associated VADM histograms for the individual periods. For the Middle–Late Pleistocene the median VADM is as high as ~7.5×10^{22} Am^2, close to the present-day dipole strength, displaying a distinct bimodal distribution with peaks at the 4–5 and 7–8 $\times 10^{22}$ Am^2 bins. When going back to the Early Pleistocene and Late Pliocene, VADMs become more concentrated at ~5×10^{22} Am^2, indicating the median of ~5×10^{22} Am^2. For the Early Pliocene the median appears to increase slightly (~6×10^{22} Am^2). However, we also can see that the distributions concentrated around ~5×10^{22} Am^2 are skewed towards lower values. We emphasize that, currently, it is difficult to say whether the average dipole strength during the Early Pliocene period was moderately high or generally consistent
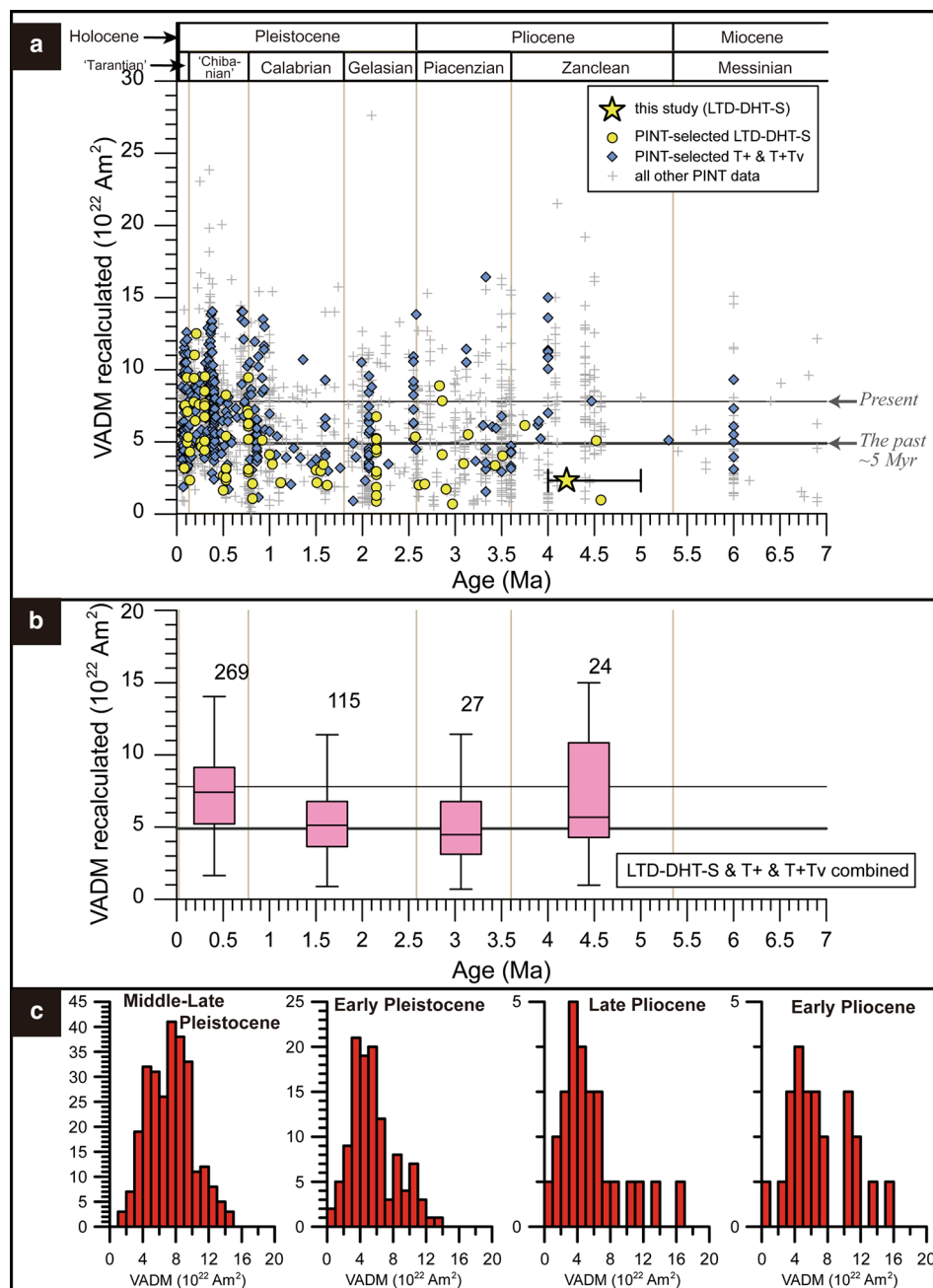
Fig. 6 Comparison of API data in VADM obtained in this study with those of the PINT database. **a** Published VADM data (recalculated in this study; grey cross symbols) for the past 7 Myr (actually 7 to 0.05 Ma), which were downloaded from the PINT database (version 2015.05; http://earth .liv.ac.uk/pint/; accessed July, 2018), represented as a VADM versus age plot together with the Baengnyeong Island data (yellow stars) from this study. Yellow circles and blue diamonds are, respectively, the LTD-DHT-S and $T+/T+Tv$ data meeting the criteria ($N_F \geq 3$, $\sigma_F \leq 20\%$ and having independent paleodirection determination, which must represent normal or reverse polarity) (see http://earth.liv.ac.uk/pint/ for the abbreviations of the PI methods). The thin (thick) horizontal line is the dipole intensity for the present-day (for the past approximately 5 Ma by Wang et al. 2015). The geologic time scales are also shown together with the abscissa axis. **b** Quartile box plots of the extracted VADM data (yellow circles and blue diamonds in Fig. 6a) including new data from this study for individual geologic time spans (0.050–0.781 Ma, 0.781–2.580 Ma, 2.580–3.600 Ma, and 3.600–5.333 Ma). Boxes represent the interquartile range, horizontal lines in the boxes are median values, and error bars represent the full range. The Arabic numeral above each upper error bar is the number used for each plot. The coordinates of boxes for *x*-axis are given arbitrarily. The thin and thick horizontal lines are same as the shown in **a**. **c** Histograms of the extracted VADMs for the individual geologic time spans (0.050–0.781 Ma, 0.781–2.580 Ma, 2.580–3.600 Ma, and 3.600–5.333 Ma)

with that over the past ~ 5 Myr ($\sim 5 \times 10^{22}$ Am^2) and thus further investigation is needed to clarify this issue.

Conclusions

From two sites of basaltic rocks with inferred ages of approximately 4–5 Ma from Baengnyeong Island, Korea, paleomagnetic and rock magnetic investigations have been performed for the first time. Paleodirectional and absolute paleointensity (API) analyses successfully reconstruct a paleomagnetic record with the VGP position at 70.2° N and 342.1° E and the VDM (VADM) of 2.87 ± 0.37 $(2.32 \pm 0.30) \times 10^{22}$ Am^2, which is considered as a normal-polarity state within the apparent secular variation range. We could confirm that, even for such samples containing non-SD particles, the Tsunakawa–Shaw (TS) API experiments can successfully give a mean API estimate with high reliability and precision. The IZZI-Thellier experiments with a bootstrap procedure in API determination gave a confirmatory result to support the TS-derived mean estimate; but the Thellier-derived value was not used in the final calculation because of the relatively large uncertainty. Our new API data from Baengnyeong Island give a fairly low dipole strength compared to the global database for the Early Pliocene, thereby indicating larger dispersion in the dipole strength during the period than found in the previous data. Further, it still cannot be certain whether the Early Pliocene dipole strength was moderately high ($> 5 \times 10^{22}$ Am^2). To clarify this ambiguity, we encourage further investigations obtaining well-determined API data of the Early Pliocene.

Abbreviations

AF: alternating field; API: absolute paleointensity; ARM: anhysteretic remanent magnetization; BDS: bulk domain stability; ChRM: characteristic remanent magnetization; FC/ZFC: in-field cooling/zero-field cooling; GAD: geocentric axial dipole; IRM: isothermal remanent magnetization; IZZI-T method: Thellier method with the IZZI protocol (Tauxe and Staudigel 2004) for absolute paleointensity determination; LTD: low-temperature demagnetization; MD: multi-domain; NRM: natural remanent magnetization; PSD: pseudo-single-domain; SD: single-domain; TRM: thermoremanent magnetization; TS method: Tsunakawa–Shaw method for absolute paleointensity determination; V(A)DM: virtual (axial) dipole moment; VGP: virtual geomagnetic pole.

Author details

[1] Geological Research Center, Geology Division, Korea Institute of Geoscience and Mineral Resources (KIGAM), Daejeon 34132, Republic of Korea. [2] Center for Advanced Marine Core Research, Kochi University, B200 Monobe, Nankoku 783-0004, Japan.

References

Ahn H-S, Kidane T, Yamamoto Y, Otofuji Y-I (2016) Low geomagnetic field intensity in the Matuyama Chron: palaeomagnetic study of a lava sequence from Afar depression, East Africa. Geophys J Int 204(1):127–146

Aitken M, Allsop A, Bussell G, Winter M (1988) Determination of the intensity of the Earth's magnetic field during archaeological times: reliability of the Thellier technique. Rev Geophys 26(1):3–12

Arai S, Kida M, Abe N, Yurimoto H (2001) Petrology of peridotite xenoliths in alkali basalt (11 Ma) from Boun, Korea: an insight into the upper mantle beneath the East Asian continental margin. J Miner Pet Sci 96(3):89–99

Biggin AJ (2006) First-order symmetry of weak-field partial thermoremanence in multi-domain (MD) ferromagnetic grains: 2. Implications for Thellier-type paleointensity determination. Earth Planet Sci Lett 245(1–2):454–470

Biggin AJ, Paterson GA (2014) A new set of qualitative reliability criteria to aid inferences on palaeomagnetic dipole moment variations through geological time. Front Earth Sci 2:24

Biggin AJ, Strik GH, Langereis CG (2009) The intensity of the geomagnetic field in the late-Archaean: new measurements and an analysis of the updated IAGA palaeointensity database. Earth Planets Space 61(1):9–22

Biggin AJ, McCormack A, Roberts A (2010) Paleointensity database updated and upgraded. Eos Trans Am Geophys Union 91(2):15

Biggin AJ, Piispa E, Pesonen LJ, Holme R, Paterson G, Veikkolainen T, Tauxe L (2015) Palaeomagnetic field intensity variations suggest Mesoproterozoic inner-core nucleation. Nature 526(7572):245

Bogue SW, Paul HA (1993) Distinctive field behavior following geomagnetic reversals. Geophys Res Lett 20(21):2399–2402

Bowles J, Gee JS, Kent DV, Bergmanis E, Sinton J (2005) Cooling rate effects on paleointensity estimates in submarine basaltic glass and implications for dating young flows. Geochem Geophys Geosyst 6(7):1–24

Choi SH, Kwon S-T (2005) Mineral chemistry of spinel peridotite xenoliths from Baengnyeong Island, South Korea, and its implications for the paleogeotherm of the uppermost mantle. Island Arc 14(3):236–253

Choi SH, Kwon S-T, Mukasa SB, Sagong H (2005) Sr–Nd–Pb isotope and trace element systematics of mantle xenoliths from Late Cenozoic alkaline lavas, South Korea. Chem Geol 221(1):40–64

Choi SH, Mukasa SB, Kwon S-T, Andronikov AV (2006) Sr, Nd, Pb and Hf isotopic compositions of late Cenozoic alkali basalts in South Korea: evidence for mixing between the two dominant asthenospheric mantle domains beneath East Asia. Chem Geol 232(3):134–151

Chough S, Kwon S-T, Ree J-H, Choi D (2000) Tectonic and sedimentary evolution of the Korean peninsula: a review and new view. Earth Sci Rev 52(1–3):175–235

Coe RS (1967) Paleo-intensities of the Earth's magnetic field determined from tertiary and quaternary rocks. J Geophys Res 72(12):3247–3262

Coe RS (1974) The effect of magnetic interactions on paleointensity determinations by the Thelliers' method. J Geomagn Geoelectr 26(3):311–317

Coe RS, Grommé S, Mankinen EA (1978) Geomagnetic paleointensities from radiocarbon-dated lava flows on Hawaii and the question of the Pacific nondipole low. J Geophys Res Solid Earth 83(B4):1740–1756

Coe RS, Riisager J, Plenier G, Leonhardt R, Krása D (2004) Multidomain behavior during Thellier paleointensity experiments: results from the 1915 Mt. Lassen flow. Phys Earth Planet Inter 147(2–3):141–153

Cogné J-P, Besse J, Chen Y, Hankard F (2013) A new Late Cretaceous to present APWP for Asia and its implications for paleomagnetic shallow inclinations in Central Asia and Cenozoic Eurasian plate deformation. Geophys J Int 192(3):1000–1024

Costin SO, Buffett BA (2004) Preferred reversal paths caused by a heterogeneous conducting layer at the base of the mantle. J Geophys Res Solid Earth 109(B6):3909–3922

Courtillot V, Gallet Y, Le Mouël J-L, Fluteau F, Genevey A (2007) Are there connections between the Earth's magnetic field and climate? Earth Planet Sci Lett 253(3–4):328–339

Cromwell G, Tauxe L, Halldórsson S (2015) New paleointensity results from rapidly cooled Icelandic lavas: implications for Arctic geomagnetic field strength. J Geophys Res Solid Earth 120(5):2913–2934

Day R, Fuller M, Schmidt VA (1977) Hysteresis properties of titanomagnetites: grain-size and compositional dependence. Phys Earth Planet Inter 13:260–267

Donadini F, Elming SÅ, Tauxe L, Hålenius U (2011) Paleointensity determination on a 1.786 Ga old gabbro from Hoting, Central Sweden. Earth Planet Sci Lett 309(3–4):234–248

Dunlop DJ (2002a) Theory and application of the Day plot (Mrs/Ms versus Hcr/Hc) 1. Theoretical curves and tests using titanomagnetite data. J Geophys Res 107(B3):2056

Dunlop DJ (2002b) Theory and application of the day plot (Mrs/Ms versus Hcr/Hc) 2. Application to data for rocks, sediments, and soils. J Geophys Res 107:2161–2174

Fabian K (2001) A theoretical treatment of paleointensity determination experiments on rocks containing pseudo-single or multi domain magnetic particles. Earth Planet Sci Lett 188(1–2):5–58

Fisher RA (1953) Dispersion on a sphere. Proceedings of the Royal Society of London. Series A Math Phys Sci 217(1130):295–305

Glatzmaier GA, Coe RS, Hongre L, Roberts PH (1999) The role of the Earth's mantle in controlling the frequency of geomagnetic reversals. Nature 401(6756):885–890

Goguitchaichvili AT, Prévot M, Camps P (1999) No evidence for strong fields during the R3–N3 Icelandic geomagnetic reversal. Earth Planet Sci Lett 167(1–2):15–34

Goguitchaichvili A, Camps P, Urrutia-Fucugauchi J (2001) On the features of the geodynamo following reversals or excursions: by absolute geomagnetic paleointensity data. Phys Earth Planet Inter 124(1):81–93

Goguitchaichvili A, Morales J, Cañon-Tapia E, Negrete R (2003) Geomagnetic field strength during late Miocene: first paleointensity results from Baja California. J Geophys Res Solid Earth 108(B2):2114

Gubbins D (1988) Thermal core-mantle interactions and time-averaged paleomagnetic field. J Geophys Res Solid Earth 93(B4):3413–3420

Gubbins D, Richards M (1986) Coupling of the core dynamo and mantle: thermal or topographic? Geophys Res Lett 13(13):1521–1524

Halls HC (1976) A least-squares method to find a remanence direction from converging remagnetization circles. Geophys J Int 45(2):297–304

Halls HC (1978) The use of converging remagnetization circles in palaeomagnetism. Phys Earth Planet Inter 16:1–11

Harrison RJ, Feinberg JM (2008) FORCinel: an improved algorithm for calculating first-order reversal curve distributions using locally weighted regression smoothing. Geochem Geophys Geosyst 9(5):Q05016

Ishikawa Y, Saito N, Arai M, Watanabe Y, Takei H (1985) A new oxide spin glass system of $(1-x)$ $FeTiO_3 - xFe_2O_3$. I. Magnetic properties. J Phys Soc Jpn 54(1):312–325

Jin MS, Kim SJ, Shin SC (1988) K/Ar and fission-track datings for volcanic rocks in the P'ohang-Kamp'o Area Research Report KR-87-27. Kor Inst Energy Resour, Seoul, pp 51–88 **(in Korean)**

Juarez MT, Tauxe L (2000) The intensity of the time-averaged geomagnetic field: the last 5 Myr. Earth Planet Sci Lett 175(3–4):169–180

Kim KH, Nagao K, Jang HS, Sumino H, Chung JI (2002) Nd, Sr and noble gas isotopic compositions of alkali basaltic rocks and mantle xenoliths in the Baegryongdo. Econ Environ Geol 35(6):523–532 **(in Korean with English abstract)**

Kim KH, Nagao K, Tanaka T, Sumino H, Nakamura T, Okuno M, Lock JB, Youn JS, Song J (2005) He–Ar and Nd–Sr isotopic compositions of ultramafic xenoliths and host alkali basalts from the Korean peninsula. Geochem J 39(4):341–356

Kirschvink J (1980) The least-squares line and plane and the analysis of palaeomagnetic data. Geophys J Int 62(3):699–718

Kitaba I, Hyodo M, Katoh S, Matsushita M (2012) Phase-lagged warming and the disruption of climatic rhythms during the Matuyama–Brunhes magnetic polarity transition. Gondwana Res 21(2–3):595–600

Kitaba I, Hyodo M, Nakagawa T, Katoh S, Dettman DL, Sato H (2017) Geological support for the Umbrella Effect as a link between geomagnetic field and climate. Sci Rep 7:40682

Kitahara Y, Yamamoto Y, Ohno M, Kuwahara Y, Kameda S, Hatakeyama T (2018) Archeointensity estimates of a tenth-century kiln: first application of the Tsunakawa–Shaw paleointensity method to archeological relics. Earth Planets Space 70(1):79

Kosterov A (2003) Low-temperature magnetization and AC susceptibility of magnetite: effect of thermomagnetic history. Geophys J Int 154(1):58–71

Laj C, Szeremeta N, Kissel C, Guillou H (2000) Geomagnetic paleointensities at Hawaii between 3.9 and 2.1 Ma: preliminary results. Earth Planet Sci Lett 179(1):191–204

Lee YS, Kodama K (2009) A possible link between the geomagnetic field and catastrophic climate at the Paleocene-Eocene thermal maximum. Geology 37(11):1047–1050

Leonhardt R, Krása D, Coe RS (2004) Multidomain behavior during Thellier paleointensity experiments: a phenomenological model. Phys Earth Planet Inter 147(2–3):127–140

Levi S (1977) The effect of magnetite particle size on paleointensity determinations of the geomagnetic field. Phys Earth Planet Inter 13(4):45–259

Lhuillier F, Shcherbakov VP, Shcherbakova VV, Ostner S, Hervé G, Petersen N (2019) Palaeointensities of Oligocene and Miocene volcanic sections from Ethiopia: field behaviour during the Cainozoic. Geophys J Int 216(2):1482–1494

Lim SB, Choi HI, Kim BC, Koh HJ (1999) Depositional system and geological structures of the Protrozoic Paegryeong Group. MOST/KIGAM, Daejeon, p 116 **(in Korean)**

Mankinen EA, Champion DE (1993) Broad trends in geomagnetic paleointensity on Hawaii during Holocene time. J Geophys Res Solid Earth 98(B5):7959–7976

McFadden PL, McElhinny MW (1982) Variations in the geomagnetic dipole 2: statistical analysis of VDMs for the past 5 million years. J Geomagn Geoelectr 34(3):163–189

Mochizuki N, Tsunakawa H, Oishi Y, Wakai S, Wakabayashi K-I, Yamamoto Y (2004) Palaeointensity study of the Oshima 1986 lava in Japan: implications for the reliability of the Thellier and LTD-DHT Shaw methods. Phys Earth Planet Inter 146(3–4):395–416

Moskowitz BM, Jackson M, Kissel C (1998) Low-temperature magnetic behavior of titanomagnetites. Earth Planet Sci Lett 157(3–4):141–149

Nagata T, Arai Y, Momose K (1963) Secular variation of the geomagnetic total force during the last 5000 years. J Geophys Res 68(18):5277–5281

Oishi Y, Tsunakawa H, Mochizuki N, Yamamoto Y, Wakabayashi K-I, Shibuya H (2005) Validity of the LTD-DHT Shaw and Thellier palaeointensity methods: a case study of the Kilauea 1970 lava. Phys Earth Planet Inter 149(3–4):243–257

Özdemir Ö, Dunlop DJ, Moskowitz BM (1993) The effect of oxidation on the Verwey transition in magnetite. Geophys Res Lett 20(16):1671–1674

Pan Y, Hill MJ, Zhu R (2005) Paleomagnetic and paleointensity study of an Oligocene-Miocene lava sequence from the Hannuoba Basalts in northern China. Phys Earth Planet Inter 151(1–2):21–35

Park J-B, Park K-H (1996) Petrology and petrogenesis of the Cenozoic alkali volcanic rocks in the middle part of Korean Peninsula (I): petrography, mineral chemistry and whole rock major element chemistry. J Geol Soc Korea 32(3):223–249 **(in Korean with English abstract)**

Paterson GA (2011) A simple test for the presence of multidomain behavior during paleointensity experiments. J Geophys Res Solid Earth 116(B10):49

Paterson GA, Tauxe L, Biggin AJ, Shaar R, Jonestrask LC (2014) On improving the selection of Thellier-type paleointensity data. Geochem Geophys Geosyst 15(4):1180–1192

Paterson GA, Biggin AJ, Hodgson E, Hill MJ (2015) Thellier-type paleointensity data from multidomain specimens. Phys Earth Planet Inter 245:117–133

Paterson GA, Muxworthy AR, Yamamoto Y, Pan Y (2017) Bulk magnetic domain stability controls paleointensity fidelity. Proc Natl Acad Sci 114(50):13120–13125

Prévot M, Mankinen EA, Coe RS, Grommé CS (1985) The Steens Mountain (Oregon) geomagnetic polarity transition: 2. Field intensity variations and discussion of reversal models. J Geophys Res Solid Earth 90(B12):10417–10448

Riisager P, Riisager J (2001) Detecting multidomain magnetic grains in Thellier palaeointensity experiments. Phys Earth Planet Inter 125(1–4):111–117

Roberts PH, Glatzmaier GA (2000) Geodynamo theory and simulations. Rev Mod Phys 72(4):1081

Rolph T, Shaw J (1985) A new method of palaeofield magnitude correction for thermally altered samples and its application to Lower Carboniferous lavas. Geophys J Int 80(3):773–781

Shaar R, Tauxe L (2013) Thellier GUI: an integrated tool for analyzing paleointensity data from Thellier-type experiments. Geochem Geophys Geosyst 14(3):677–692

Shaar R, Ron H, Tauxe L, Kessel R, Agnon A (2011) Paleomagnetic field intensity derived from non-SD: testing the Thellier IZZI technique on MD slag and a new bootstrap procedure. Earth Planet Sci Lett 310(3–4):213–224

Shaw J (1974) A new method of determining the magnitude of the palaeomagnetic field: application to five historic lavas and five archaeological samples. Geophys J Roy Astron Soc 39(1):133–141

Shin H-J, Kil Y-W, Jin M-S, Lee S-H (2006) Petrological study on upper mantle xenoliths from Asan and Pyeongtaek area. J Geol Soc Korea 42(1):95–113 **(in Korean with English abstract)**

Skumryev V, Blythe HJ, Cullen J, Coey JMD (1999) AC susceptibility of a magnetite crystal. J Magn Magn Mater 196–197:515–517

Sprain CJ, Feinberg JM, Geissman JW, Strauss B, Brown MC (2016) Paleointensity during periods of rapid reversal: a case study from the Middle Jurassic Shamrock batholith, western Nevada. Geol Soc Am Bull 128(1–2):223–238

Tanaka H, Kobayashi T (2003) Paleomagnetism of the late Quaternary Ontake Volcano, Japan: directions, intensities, and excursions. Earth Planets Space 55(4):189–202

Tarduno JA, Cottrell RD, Watkeys MK, Bauch D (2007) Geomagnetic field strength 3.2 billion years ago recorded by single silicate crystals. Nature 446(7136):657

Tarduno JA, Cottrell RD, Watkeys MK, Hofmann A, Doubrovine PV, Mamajek EE, Liu D, Sibeck DG, Neukirch LP, Usui Y (2010) Geodynamo, solar wind, and magnetopause 3.4 to 3.45 billion years ago. Science 327(5970):1238–1240

Tarduno JA, Cottrell RD, Davis WJ, Nimmo F, Bono RK (2015) A Hadean to Paleoarchean geodynamo recorded by single zircon crystals. Science 349(6247):521–524

Tauxe L, Staudigel H (2004) Strength of the geomagnetic field in the Cretaceous Normal Superchron: new data from submarine basaltic glass of the Troodos Ophiolite. Geochem Geophys Geosyst 5(2):Q08H13

Tauxe L, Gans P, Mankinen EA (2004) Paleomagnetism and 40Ar/39Ar ages from volcanics extruded during the Matuyama and Brunhes Chrons near McMurdo Sound, Antarctica. Geochem Geophys Geosyst. https://doi.org/10.1029/2003gc000656

Tauxe L, Shaar R, Jonestrask L, Swanson-Hysell N, Minnett R, Koppers A, Constable C, Jarboe N, Gaastra K, Fairchild L (2016) PmagPy: software package for paleomagnetic data analysis and a bridge to the Magnetics Information Consortium (MagIC) Database. Geochem Geophys Geosyst 17(6):2450–2463

Thébault E, Finlay CC, Beggan CD, Alken P, Aubert J, Barrois O, Bertrand F, Bondar T, Boness A, Brocco L (2015) International geomagnetic reference field: the 12th generation. Earth Planets Space 67(1):1–19

Thellier E, Thellier O (1959) Sur la direction du champ magnetique terrestre dans le passe historique et geologique. Annal Geophys 15:285–375

Tsunakawa H, Shaw J (1994) The Shaw method of palaeointensity determinations and its application to recent volcanic rocks. Geophys J Int 118(3):781–787

Valet JP, Brassart J, Le Meur I, Soler V, Quidelleur X, Tric E, Gillot PY (1996) Absolute paleointensity and magnetomineralogical changes. J Geophys Res Solid Earth 101(B11):25029–25044

Wang H, Kent DV (2013) A paleointensity technique for multidomain igneous rocks. Geochem Geophys Geosyst 14(10):4195–4213

Wang H, Kent DV, Rochette P (2015) Weaker axially dipolar time-averaged paleomagnetic field based on multidomain-corrected paleointensities from Galapagos lavas. Proc Natl Acad Sci 112(49):15036–15041

Xu S, Dunlop DJ (2004) Thellier paleointensity theory and experiments for multidomain grains. J Geophys Res Solid Earth. https://doi.org/10.1029/2004JB003024

Yamamoto Y, Hoshi H (2008) Paleomagnetic and rock magnetic studies of the Sakurajima 1914 and 1946 andesitic lavas from Japan: a comparison of the LTD-DHT Shaw and Thellier paleointensity methods. Phys Earth Planet Inter 167(1):118–143

Yamamoto Y, Tsunakawa H (2005) Geomagnetic field intensity during the last 5 Myr: LTD-DHT Shaw palaeointensities from volcanic rocks of the Society Islands, French Polynesia. Geophys J Int 162(1):79–114

Yamamoto Y, Yamaoka R (2018) Paleointensity study on the Holocene surface lavas on the island of Hawaii using the Tsunakawa–Shaw method. Front Earth Sci 6:48

Yamamoto Y, Tsunakawa H, Shibuya H (2003) Palaeointensity study of the Hawaiian 1960 lava: implications for possible causes of erroneously high intensities. Geophys J Int 153(1):263–276

Yamamoto Y, Shibuya H, Tanaka H, Hoshizumi H (2010) Geomagnetic paleointensity deduced for the last 300 kyr from Unzen Volcano, Japan, and the dipolar nature of the Iceland Basin excursion. Earth Planet Sci Lett 293(3–4):236–249

Yamamoto Y, Torii M, Natsuhara N (2015) Archeointensity study on baked clay samples taken from the reconstructed ancient kiln: implication for validity of the Tsunakawa–Shaw paleointensity method. Earth Planets Space 67(1):63

Yamazaki T, Yamamoto Y (2014) Paleointensity of the geomagnetic field in the Late Cretaceous and earliest Paleogene obtained from drill cores of the Louisville seamount trail. Geochem Geophys Geosyst 15(6):2454–2466

Yu Y, Tauxe L (2005) Testing the IZZI protocol of geomagnetic field intensity determination. Geochem Geophys Geosyst 6(5):53

Yu Y, Tauxe L, Genevey A (2004) Toward an optimal geomagnetic field intensity determination technique. Geochem Geophys Geosyst. https://doi.org/10.1029/2003gc000630

Ziegler L, Constable C, Johnson C, Tauxe L (2011) PADM2M: a penalized maximum likelihood model of the 0–2 Ma palaeomagnetic axial dipole moment. Geophys J Int 184(3):1069–1089

Zijderveld JDA (1967) A. C. demagnetization of rocks: analysis of results. Elsevier, Amsterdam

Publisher's Note